

Analytical coarse grained potential parameterization by Reinforcement Learning for anisotropic cellulose

Don Xu

keywords: Reinforcement Learning, Boltzmann inversion, coarse grained,
cellulose, anisotropy, hydrogen bond

Abstract

Cellulose nanocrystals(CNC) is a nano form of cellulose with great mechanical performance and other merit attributes. Revealed by preceding researches of experiments and molecular simulations, CNC has an anisotropic structure, in which hydrogen bonds play a pivotal role. Understanding structure and mechanical behavior of CNC in a mesoscopic scale is critical to improve manufacturing process and property of final products, in which experiment observation and atomistic simulation are not appropriate. Reinforcement Learning (RL) has been an important power source for many industrial and academic achievements in lots of fields. Nevertheless, the potential of RL has not been fully utilized in molecular dynamics (MD) simulations. In this work, we introduce an analytical coarse grained (CG) potential directly parameterized by RL. We utilize RL and Boltzmann inversion to develop a novel CG model of cellulose with consideration of anisotropy and other properties like polymer stiffness. Resultant CG model is not limited to target properties for training, and it could present mechanical properties under other circumstances without additional training. With a little help of prior physical knowledge, the results show that RL could help us parameterize potentials and help us better understand the interactions among particles. Our model illustrates the capability of RL to construct a CG potential which are physically explainable and powerful.

Introduction

1.1 Cellulose nanocrystals

As the most opulent natural polymer resources on earth with many natural sources like wood, bamboo, algae and bacteria, cellulose is widely available and eco-friendly^[1;2]. Cellulose has many merit attributes like renewability, low-cost, biocompatibility, biodegradability, and good mechanical performance^[3;4], which make it a good replacement for petroleum-based materials. As a nano form of cellulose materials, cellulose nanocrystals (CNC) could achieve superior performance, like high elastic modulus (about 200 GPa), low mass density (1.6 g/cm³), high specific surface area (several hundreds of m²/g) and low coefficient of thermal expansion^[4]. CNC have been widely researched to prepare advanced materials considering their brilliant mechanical properties and interactions with other ions or polar molecules^[5], for applications like biomedicine^[6], water treatment^[7], energy storage^[8] and humidity sensor^[9]. Computation simulations including ab initio simulations^[10], molecular dynamics^[11] and finite element method^[12] are performed to reveal molecular details and kinetics of CNC. Concentrating on the mechanical properties of CNC, analysis from the experimental^[13–15], computational simulation^[12;16;17] and

analytical^[18;19] opinions are all reported. Hydroxyls and hydrogen bonds usually play a pivotal role in these behaviors^[20–22].

CNC are composed of parallel cellulose chains, and axial elastic modulus are much larger than transverse modulus cause covalent bonds are much stronger than van der Waals and hydrogen bonding interactions. Axial modulus and transverse modulus of CNC is about 100-200 GPa and 10-50 GPa, which is confirmed by experiments^[4] and simulations^[16;17]. The complanate sidechains and hydrogen bonds are key factors for the transverse anisotropy of CNC. In cross section, CNC are orthotropic and have three characteristic load directions: along the hydrogen bonding plane, perpendicular to hydrogen bonding plane and slant to hydrogen bonding plane (Figure 1). Xiawa Wu et al. emphasized the anisotropy of CNC, and they simulate the stretch in the three orthogonal directions (along the chain, parallel and perpendicular to hydrogen bonding planes) at three different strain rates and find that the mechanical properties (like elastic modulus and Poisson's ratio) are highly anisotropic and independent of strain rate^[17]. When a vertical load is applied, the slant CNC model undergoing an obvious frictional sliding are tough while the vertical and horizontal model are just fragile. Frictional sliding is important mechanical behavior for CNC and elucidated in former papers. Xiawa Wu et al. simulate the inter layer frictions of two cellulose layers under different velocities, normal loads and relative angles, and they find that hydrogen bonds and inter layer distance are important factors^[23]. Chi Zhang et al. systematically simulate and examine the impact of loading direction, interfacial moisture and misalignment on the CNC-CNC interface friction mechanical behavior and they find that the density of hydrogen bonds is strongly correlated with the interaction energy^[24]. The frictional sliding of CNC when loading direction is slant to hydrogen bonding planes are critical.

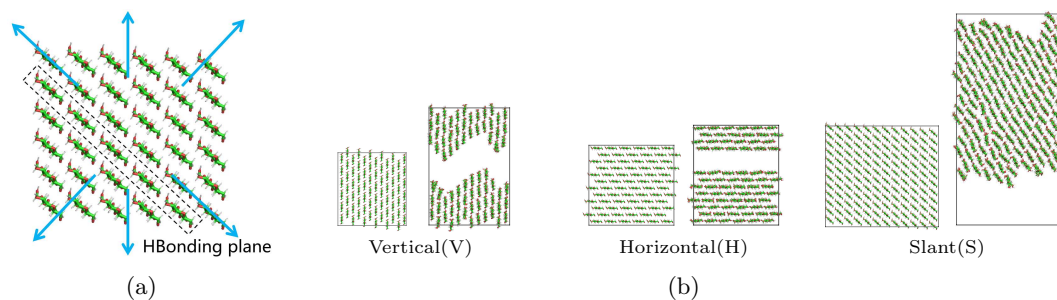


Figure 1: Orthotropic cross section and characteristic directions. (a) Characteristic directions for the orthotropic cross section which is dominated by hydrogen bonding planes. (b) Characteristic behaviors. The complanate sidechains and hydrogen bonds are critical for the anisotropy of CNC. The vertical model and horizontal model are dominated by hydrogen bonds and Van der Waals interactions respectively, presenting fragile performances. The load of slant model corresponding to CNC under stretch, inducing complanate sidechains frictions and rotations.

To reflect the performance of CNC in a larger length scale, there are many CG models developed with different CG level for different purposes like mechanical properties and molecular interactions^[25]. Phenomenon like self-assembly or nano cellulose network require supra CG models, which means several cellulose residues become one bead^[26–28] If mechanical properties of CNC is considered, one cellulose residue (one residue or two nearby residues in a same chain) is usually CG into a bead^[29;30], neglecting directionality of cross sections. Some researchers lay stress on the molecular details and interactions, thus they will preserve more molecular details and they coarse grain a cellulose residue into more than one bead instead of several residues into one bead^[31–34].

However, the CG models of cellulose mentioned before could not reveal the hydrogen bond interactions and resultant directionality. A few works present the directionality by anisotropic

particles^[26;35] or additional bonds which are not backed by real molecular structure^[36-39]. Mehdi Shishehbor et al. develop CG CNC by matching axial elastic modulus and transverse stress-strain curve to research the interface interaction and failure mechanism^[38]. Their CG mapping neglects complanate sidechains of cellulose, and they add additional bonds between beads to compensate its lack of directionality. Although less important in their cases, anisotropic particles and the bonded directionality is not suitable if considering transverse failure mechanism with frictional sliding involved. Nonetheless presenting kinetics like energy and mechanical properties are challenging in CG models^[33].

1.2 Machine Learning parameterization and Reinforcement Learning

When thinking about Machine Learning and force field, data-driven Machine Learning potential may be the first thing comes to mind nowadays. Machine learning models especially neural networks models could describe interactions among particles without too much substantial physical/chemical intuition^[40;41]. However, significant problems are still open for machine learning potentials, like long-ranged interactions, transferability and kinetics (especially for CG models) are still open^[40]. Neural networks models also have problems of explainability^[42] and computational cost. On the other hand, machine learning methods could also be utilized to parameterize analytical force fields^[43;44]. Bayesian optimization^[45], Particle Swarm Optimization^[46], Genetic algorithm^[47], Kernel function^[48], Simplex algorithm^[47] and Monte Carlo Tree Search^[49] are used to parameterize analytical CG potentials.

Employment of RL in CG simulations and potential parameterization are still on the early stage^[49]. RLCG by Shenghao Wu et al. integrates graph attention neural networks and RL to learn CG mappings^[50]. Anirban Chandra et al. uses continuous action Monte Carlo Tree Search^[51] powered by RL to parameterize analytical hybrid bond-order coarse-grained force field to simulate aggregations of liquid-liquid mixtures^[49]. RL is based on biomimetics, intuitively imitating the learning of creatures, promising in Markov decision processes for decision-making, control and optimization^[52;53]. Model-free RL algorithm could deal with strongly non-linear problems without prior expert knowledge, it could automatically carry out trial-and-error learning procedures. More information of RL scheme is presented in Methods section.

In summary, complanate sidechains and hydrogen bonding interactions are key features of CNC orthotropic cross section and corresponding transverse mechanical behaviors, which are not well described in former CG models. With a tight budget of computation cost and a wish of better explainability, transferability and kinetics, a carefully designed model with explicit analytical potential instead of a data-driven machine learning potential model is determined to reproduce orthotropic mechanical behavior of CNC. In this paper, we introduce a RL parameterized novel CNC CG model with a well consideration of complanate sidechains, hydrogen bonds and other molecular attributes like polymer stiffness and axial stretch. And the hydrogen bonds are implemented as nonbonded interactions, not as additional bonds.

Methods

2.1 Mapping and topology

As shown in Figure 2, in this model, one cellulose residue are mapped into three different beads. The bead one the backbone is called as CL1, where the beads on the side chains are called CL2 and CL3. This mapping stresses complanate sidechains of cellulose chains and inter chain hydrogen interactions. Two features are considered: the distance of CL2 to CL3 in

a residue and the angle of CL2-CL3 and backbone. The first distance feature should be long enough to bear torque and present coplanate sidechains while the second angle feature are expected to be close to right angle. When in the crystal states, the angle of nearby CL2:CL3-CL1(Blue:Orange-Green) or CL3:CL2-CL1(Orange:Blue-Green) (colon means these two beads are not bonded together while dash means bonded) are close to 180° , which are illustrated in Figure 2.

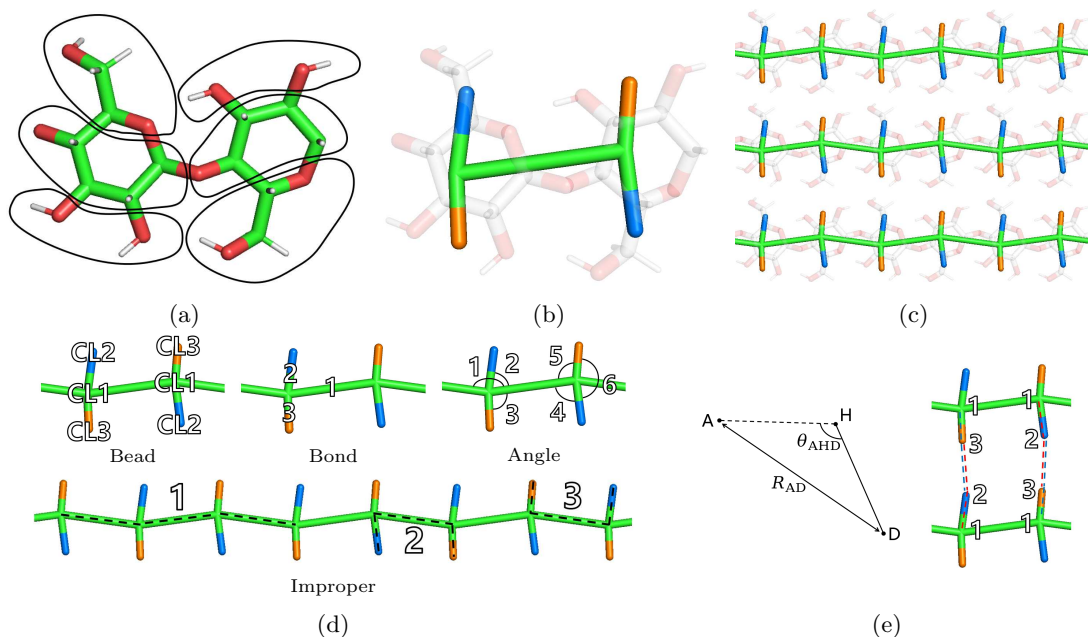


Figure 2: Mapping and topology. (a) Mapping and (b)(c) mapped overlay. One cellulose residue are mapped into three different beads: CL1 on the backbone, CL2 and CL3 on the side chains. The basic idea of this mapping is to preserve coplanate structure and hydrogen bonds within a hydrogen bonding layer. Qualitatively, the distance of CL2 to CL3 from a same residue is desired to be large enough and the side chain beads are expected to be perpendicular to backbones. Under this mapping, a layer of CNC will be mapped as a network-like structure where inter chain interactions are stressed. (d) Bonded topology. Bonded interactions are required to preserve molecular structure and performances of stretch, bend and torsion. (e) Nonbonded topology. For HB potentials, two symmetric Acceptor:Hydrogen-Donor relations (CL2:CL1-CL3 and CL3:CL1-CL2) are defined to present inter chain hydrogen bonds. The HB potentials are determined by both A:D distance and A:H-D angle.

Based on this mapping, we apply 3 types of bonds, 6 types of angles and 3 types of improper dihedrals to present the bonded interactions (Figure 2). Bonds, angles and improper dihedrals are designed to simulate and restrain deformation of stretch, bend and torsion of a cellulose chain. To assure restraints in a non-periodic chain (which is used for polymer stiffness screening), CL2-CL1-CL1 angles and CL3-CL1-CL1 angles are categorized into two types respectively. One directional nonbonded three-body interaction is introduced to describe inter chain hydrogen bonds, requiring definitions of Acceptor, Hydrogen and Donor. Two A:H-D topologies are determined given the importance of hydrogen bonding and symmetries: CL2:CL1-CL3 and CL3:CL1-CL2. This directional interaction is impacted by A:H-D angle^[54] and A-D distance.

2.2 Potentials

In this model, the potential energy contains both bonded and nonbonded interactions:

$$V_{System} = V_{Bond} + V_{Angle} + V_{Improper} + V_{Nonbonded} \quad (1)$$

. The bonded interactions are all in the harmonic style

$$V_{Bond} = \sum k_{B,i}(r - r_{0,i})^2 \quad (2)$$

$$V_{Angle} = \sum k_{A,i}(\theta - \theta_{0,i})^2 \quad (3)$$

$$V_{Improper} = \sum k_{I,i}(\chi - \chi_{0,i})^2 \quad (4)$$

, while the nonbonded interactions contain Lennard-Jones (LJ) potentials and hydrogen bond (HB) potentials^[55],

$$V_{Nonbonded} = \sum V_{LJ,i} + \sum V_{HB,i} \quad (5)$$

in which V_{LJ} and V_{HB} are in the forms

$$V_{LJ} = \begin{cases} \epsilon_L [4(\frac{\sigma_L}{r})^{12} - 4(\frac{\sigma_L}{r})^6] + V_{shift} & , r < r_{in} \\ \int_{r_{in}}^r [C_1 + C_2(x - r_{in}) + C_3(x - r_{in})^2 + C_4(x - r_{in})^3] dx + V_0 & , r_{in} < r < r_c \end{cases} \quad (6)$$

$$V_{HB} = \begin{cases} \epsilon_H [5(\frac{\sigma_H}{r})^{12} - 6(\frac{\sigma_H}{r})^{10}] \cos^n(\theta - \theta_0 + \pi) & , r < r_{in} \quad \text{and} \quad \theta - \theta_0 + \pi > \theta_c \\ S(i) \cdot \epsilon_H [5(\frac{\sigma_H}{r})^{12} - 6(\frac{\sigma_H}{r})^{10}] \cos^n(\theta - \theta_0 + \pi) & , r_{in} < r < r_{out} \quad \text{and} \quad \theta - \theta_0 + \pi > \theta_c \end{cases} \quad (7)$$

where:

$$S(i) = \frac{(r_{out}^2 - r^2)^2 [r_{out}^2 + 2r^2 - 3r_{in}^2]}{(r_{out}^2 - r_{in}^2)^3} \quad (8)$$

The LJ potential is a 12-6 formula of Lennard-Jones interactions and the HB potential is in 12-10 formula with scaling by power of cosine of A:H-D angle: Technically they are pair style lj/smooth with shift and a modified version of pair style hbond/dreiding/lj of LAMMPS^[54] respectively. lj/smooth is designed to smooth force to zero at the cutoff radius using a polylinear expression; this modified version of hbond/dreiding/lj ensures that potential energy reach minima at θ_0 instead of π . Energy and force curves of HB and LJ potential are enclosed in Supplementary Figure S1.

The equilibrium acceptor:hydrogen-donor angles in this CG mapping are close to π . Even though we generalize it by adding an equilibrium angle of A:H-D, an equilibrium angle close to π is suggested to stabilize conical energy surface.

2.3 Boltzmann inversion for harmonic potential

Boltzmann inversion is structure-based and widely utilized to determine bonded potentials. It could also be integrated with machine learning methods to construct potentials^[46;56] or used as benchmarks^[57;58].

For a harmonic potential following Boltzmann distribution, where the bond length (or angle, or dihedral) is a deviated x around equilibrium length x_0 :

$$\rho(x + x_0) \propto e^{-\frac{V}{k_B T}} = e^{-\frac{V_x - V_0}{k_B T}} = e^{-\frac{kx^2}{2k_B T}} \quad (9)$$

. Mark $\rho(x_0) = \rho_0$:

$$\begin{aligned} \ln \rho(x + x_0) &= -\frac{kx^2}{2k_B T} + \ln \rho_0 \\ k &= -2k_B T \cdot \frac{d[\ln \rho(x + x_0)]}{d[x^2]} \end{aligned} \quad (10)$$

. Then mark $\frac{d[\ln \rho(x+x_0)]}{d[x^2]}$ as κ :

$$k = -2k_B T \cdot \kappa \quad (11)$$

However, the k derived directly need to be reparameterized^[49;59;60] to present performances cause Boltzmann distribution is relative intrinsically. The effective k is k_0 times of κ :

$$k_i = k_0 \kappa_i \quad (12)$$

. Based on κ of each other, three k are utilized for bond, angle and improper one by one. As a result, there is one bond k_{B0} , one angle k_{A0} and one improper k_{I0} . k_{B0} , k_{A0} and k_{I0} are determined by RL optimization with consideration of axial elastic modulus, persistence length and end to end distance.

2.4 Reinforcement Learning and degenerate RL

In RL, the whole problem is named as environment and the optimization program is called anthropologically as Agent. Environment provides at least three types of information: observation, action space and reward. In an interaction episode with the environment, agent will get a partial observation o_t of the environment state, then it picks one action a_t in the action space. The action by agent will impact the environment evolution and be evaluated by a reward r_t function. By continuously interacting with the environment, the agent will gradually learn how to take action corresponding to a given observation in order to get maximized cumulated reward

$$R(\tau) = \sum_{t=0}^{\infty} \gamma^t r_t \quad (13)$$

, where $\gamma \in (0, 1)$ is a discount factor.

In this paper, a degenerate version of RL in a one-shot diagram is leveraged. There is only one step in a learning episode and only one reward is sampled

$$R(\tau) = r_0 \quad (14)$$

cause the performance of a set of coefficients are independent of any others. Consequently, RL algorithm is exploited as a non-linear optimizer, guided under indirect supervision by a reward function. This exploitation approach of RL is inspired by Jonathan Viquerat et al.^[61], which is quite rare especially for potential parameterization.

The RL agent in this work is powered by Soft Actor Critic (SAC) algorithm^[62]. SAC is the recommended state-of-the-art algorithm for continuous action space by the doc of OpenAI Stable-Baselines3^[63]. The key feature of SAC is a trade-off between expected reward and entropy, which

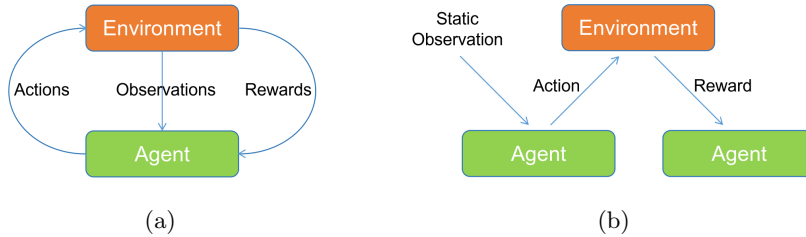


Figure 3: RL diagrams. (a) RL standard diagram. In the standard diagram of RL, agent will interact with environment continuously, taking actions corresponding to observations. Its optimization target is to maximize cumulative reward $R(\tau) = \sum_{t=0}^{\infty} \gamma^t r_t$. (b) RL one-shot diagram. However, one-shot diagram is applied in this paper and only one episode is processed. In this case, RL is employed as a nonlinear optimizer with the guidance of its reward function.

means SAC policy will preserve randomness to a certain extent in its actions. SAC is a gradient-free and model-free method which means it does not rely on specific problem environment and it could deal with strongly non-linear problems after enough training. Detailed information of SAC could be obtained in the doc of OpenAI Stable-Baselines3^[63].

When training, agent action consists of 17 normalized coefficients ranging in $[-1,1]$ cause most RL algorithms rely on a standard normal distribution^[63]. Actions will be transformed linearly into physical space corresponding to 3 bonded k , 1 HB ϵ , 1 HB σ , 6 LJ ϵ and 6 LJ σ . The Reward function is the critical factor to guide the learning of agent, and it is defined by a series of match degrees. Match degree m is defined as

$$m = \frac{1}{1 + \left| \frac{y_1 - y_0}{y_0} \right|} \quad (15)$$

with a threshold m_t

$$M = \begin{cases} m & , m \geq m_t \\ 0 & , m < m_t \end{cases} \quad (16)$$

, where y_0 stands for the reference value and y_1 for the sampled value. The Reward function is a sum of a series of match degree except for transverse strength M_s and toughness M_t ,

$$Reward = \sum M_i + w \cdot \min(M_s, M_t) \quad (17)$$

cause we noticed it that match degree of transverse strength and toughness are the hardest to match. In RL, reward functions are required not only to be accurate but also to be discriminant enough^[64]. Weight of M_s/M_t and threshold are designed to enhance discrimination.

2.5 Simulation setup

For both all atom (AA) and coarse grained (CG) simulations, three models of different arrangement directions with stretch load in the vertical direction are simulated under NPT ensemble at 0.1 MPa. AA simulations are all performed using GROMACS^[65;66] software with CHARMM36^[67;68] force field (force field files are generated by CHARMM-GUI tools^[69;70]). CG simulations are all performed using LAMMPS^[54] with self-defined force field. Based on the performance curve by Robert Sinko et al^[71], we decide to use a CNC which contains 144 cellulose chains. To reduce computational cost, the vertical and horizontal model which represent fragile

fracture only contains 72 cellulose chains. Stretch load are applied using cell deformation at constant speed 10.0 nm/ns. 100 replica AA simulations with different stretch speed ranging from 0.1 nm/ns to 40.0 nm/ns are performed. AA simulation results confirm that sampled strength and toughness are stable in this speed range, whose average value deviations are less than 15% (Supplementary Figure S3 and Figure S4).

2.6 Training procedures and statistics-guided reduction

Before training, equilibrium geometry parameters (bond length l^e /angle size θ^e /dihedral size χ^e) are directly deprived from mapped AA simulation, and estimated force constants for bonded harmonic interactions are determined by Boltzmann inversions. 3 rescale factors are still needed for bond, angle and improper but their relative ratios are kept (for example, that means all force constants for improper are rescaled with the same factor). As we introduced before, there are 17 coefficients where 3 are bonded coefficients and 14 are nonbonded coefficients. To simplify the problem and reduce the computational cost, three stages of training are designed (Figure 4): The first stage are bonded only training for 3 bonded k , ignoring all nonbonded interactions and targeting at bonded properties including axial elastic modulus and polymer stiffness, cause we cannot determine the influence of nonbonded interactions and we assume they are not critical here. The second stage are nonbonded training for 14 nonbonded coefficients with all bonded coefficients from first stage, targeting at both bonded properties and nonbonded properties (transverse strength and toughness in three characteristic directions). The third stage are preserved only if performances in the second stage is not satisfying enough, and it will consider all 17 coefficients and target at all performances at every turn.

The results elucidated that nonbonded interactions do not play a pivotal role for bonded properties and our training ended in the second stage.

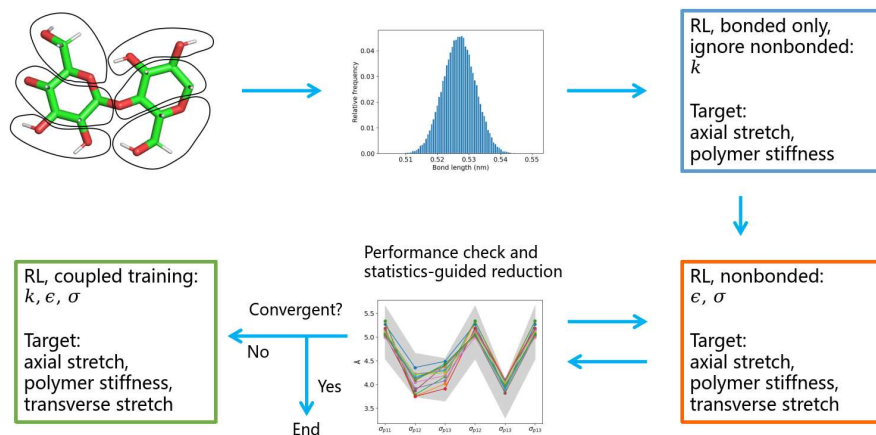


Figure 4: Training procedures. Bonded properties (axial elastic modulus and polymer stiffness) and nonbonded properties (transverse strength and toughness in characteristic directions) are target attributes. Before training, equilibrium bonded geometry parameters and force constants of bonded harmonic potentials are estimated by mapped AA simulations using Boltzmann inversion. Then force constants are scaled later by RL in the bonded only training to present bonded properties in the first stage. In bonded only training, all nonbonded interactions are ignored as we assume that nonbonded interactions do not matter much in this case. Given both bonded and nonbonded properties, nonbonded training using bonded coefficients obtained before are performed to match both bonded and nonbonded properties. Only one simulation is performed for each target properties respectively in the training, thus transverse stretch performances are manually checked with replica simulations to confirm agreement of transverse performance distributions. Multiple sets of coefficients are collected to find key coefficients and reduce the number of independent coefficients for computational cost and physical explainability. Results confirm that our assumption for bonded properties are reasonable thus actually the coupled training are never performed.

However, there is one important artificial experience intervention in the training process. Limited by computational cost, the transverse stretch performance is sampled only once which could not ensure the performance distribution alignment between AA and CG models. Thus, manual test for optimized coefficients are required to check the performance distribution, and statistics of several optimized coefficients are performed inspired by Bridgette J. Befort et al^[44]. The coefficients whose distribution is quite deviated are seen as unimportant factors, and only the coefficients with obvious tendency are kept as independent coefficients. These statistics-guided reduction procedures will be described in Results section.

Results

3.1 Coefficients

Distance coefficients σ of nonbonded interactions are estimated by equilibrium distance of mapped AA simulation results. The definition of equilibrium distance d^e is the average of minimum distance for nonbonded bead pairs

$$d^e = \langle d_m^e \rangle = \langle \min(d_{mn}^e) \rangle \quad (18)$$

. For a CL1 bead, there are many CL1 beads around itself which are not connected by bonds, and the minimum distance $d_m^e = \min(d_{mn}^e)$ is sampled. The average value $d^e = \langle d_m^e \rangle$ of all minimum nonbonded distances and all trajectories are defined as equilibrium distances. As AA and CG simulation are performed in NPT ensemble at 0.1 MPa, initial guess of nonbonded considering the stationary point of LJ potential σ is ranged in $[0.89d^e, 1.00d^e]$, which contains $2^{-\frac{1}{6}}d^e$. And this range is extended to symmetric $[0.89d^e, 1.11d^e]$ as the action space.

The training of coefficients is done by several training loops, each contains 1024 training steps. When a training loop is finished, its agent information will be saved and loaded by later training. Comparing to the first training loop, last training loop will achieve high reward much faster and its average reward will be much more stable (Figure 5a). More quantitatively, average reward and max reward of different training loop are compared (Figure 5b) to confirm the convergence of training.

When the training is confirmed to be convergent, statistics of coefficients with highest reward in every training loops is executed to find important coefficients. The first reduction of nonbonded coefficients is physics-informed:

$$\sigma_{p11} = \sigma_{p22} = \sigma_{p33} \quad (19)$$

, where σ_{p11} means distance coefficient of CL1-CL1 nonbonded interactions. The degree of freedom of CG model is obviously less than its original AA model. In this case, an important impact of more orderly structure is noticed: the equilibrium distance of same beads should be quite close. In other words, equilibrium distance of CL1-CL1, CL2-CL2 and CL3-CL3 are quite close while in the mapped AA simulations does not present. Thus we choose the *equilibrium distance* of ideal crystal structure as σ estimations instead of well relaxed structures or characteristic distances of radial distribution functions. The first physics-informed restraint is also beneficial to reproduce fragile fracture in vertical and horizontal models.

Later reduction of nonbonded coefficients is statistics-based.

Second reduction: comparing to d^e , only σ_{p23} has an unexpected intention to be larger than it, keep only σ_{p11} and σ_{p23} independent only:

$$\sigma_{p12} = \frac{d_{p12}^e}{d_{p11}^e} \sigma_{p11}, \sigma_{p23} = \frac{d_{p23}^e}{d_{p11}^e} \sigma_{p11}, \sigma_{p13} = \frac{d_{p13}^e}{d_{p11}^e} \sigma_{p11} \quad (20)$$

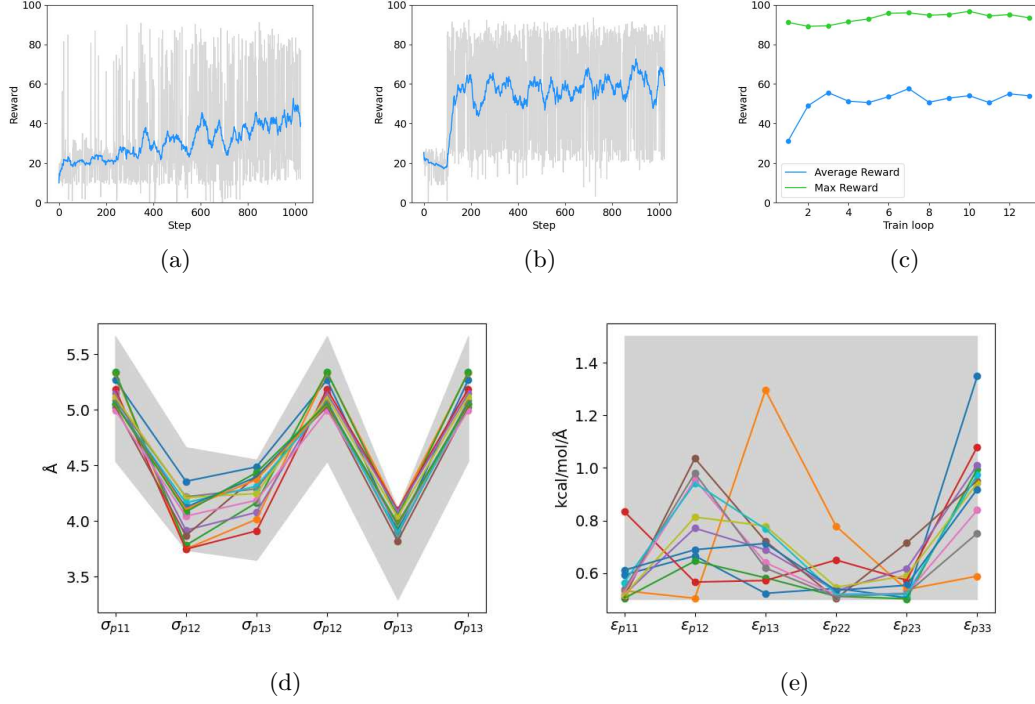


Figure 5: Training convergence and statistics-guided reduction. (a) Reward and its moving average in the first and (b) the last training loop. One training loop contains 1024 training steps, and later training loop is based on former training loops. Average reward are higher and stable in later training loops. (c) Average and max reward of different training loops. Average reward and max reward are both convergent after enough training. After training, best coefficients of different training loops will be collected to do statistics-guided reduction. The first reduction is inferred from geometry characteristics of CG models, and a constraint of $\sigma_{p11} = \sigma_{p22} = \sigma_{p33}$ is applied (pnn stands for pair of CLm and CLn), which is also helpful to the fragile behavior in vertical and horizontal directions. (d) The second reduction is about distance coefficients by statistics. σ except for σ_{p23} oscillates around equilibrium distance d^e while an obvious enlargement of σ_{p23} is observed. Then only σ_{p11} and σ_{p23} are kept as independent distance coefficients: $\sigma_{p12} = \frac{d^e}{d^e} \sigma_{p11}, \sigma_{p13} = \frac{d^e}{d^e} \sigma_{p11}$. (e) The third reduction is about energy coefficients by statistics. After first and second reduction, we notice that ϵ_{p23} is usually the smaller one in energy coefficients, which may correspond to the σ_{p23} enlargement. Then only ϵ_{p23} and ϵ_{p23} are kept as independent energy coefficient: $\epsilon_{p11} = \epsilon_{p22} = \epsilon_{p33} = \epsilon_{p12} = \epsilon_{p13}$.

Third reduction: ϵ_{p23} are usually the smallest energy coefficients in the system, trying to keep only ϵ_{p11} and ϵ_{p23} independent only:

$$\epsilon_{p11} = \epsilon_{p22} = \epsilon_{p33} = \epsilon_{p12} = \epsilon_{p13} \quad (21)$$

After these dimensionality reduction, only 7 independent coefficients are preserved: 3 bonded k , 1 HB ϵ , 1 HB σ , 1 LJ ϵ and 1 LJ σ .

Coefficients are determined and shown in 1 and 2. All coefficients are given with 4 significant digits.

Table 1: Bonded coefficients

type	id	$k(\text{kcal/mol}/\text{\AA}^2)$	$l_0(\text{\AA})$	$l_{AA}^e(\text{\AA})$	$l_{CG}^e(\text{\AA})$
bond	1	64.06	5.270	5.270	5.258
	2	82.42	2.493	2.493	2.472
	3	112.3	2.066	2.066	2.061
		$k(\text{kcal/mol})$	$\theta_0(^{\circ})$	$\theta_{AA}^e(^{\circ})$	$\theta_{CG}^e(^{\circ})$
angle	1	30.97	163.5	163.5	162.3
	2	38.79	74.2	74.2	74.7
	3	30.52	93.2	93.2	94.0
	4	27.28	90.0	90.0	89.2
	5	25.97	102.0	102.0	101.4
	6	22.42	166.3	166.3	165.1
		$k(\text{kcal/mol})$	$\chi_0(^{\circ})$	$\chi_{AA}^e(^{\circ})$	$\chi_{CG}^e(^{\circ})$
improper	1	0.1702	178.0	178.0	180.0
	2	0.1555	2.3	2.3	0.0
	3	0.1698	2.9	2.9	0.0

Table 2: Nonbonded coefficients

type	pair	$\epsilon(\text{kcal/mol}/\text{\AA})$	$\sigma(\text{\AA})$	$d_{AA}^e(\text{\AA})$	$d_{CG}^e(\text{\AA})$
HB	2:1-3	1.404	6.017		
	3:1-2	1.404	6.017		
LJ	1-1	0.9031	5.101	5.397	5.750
	1-2	0.9031	4.201	4.769	4.473
	1-3	0.9031	4.101	4.712	4.609
	2-2	0.9031	5.101	4.636	5.260
	2-3	0.5031	4.083	3.983	4.018
	3-3	0.9031	5.101	4.528	5.271

3.2 Bonded properties

For bonded interactions or the validation check of bonded coefficients, we consider the axial elastic modulus and the polymer stiffness of a single cellulose chain (Table 3 and Figure 6).

Polymer stiffness of cellulose chains contains 10, 20 and 30 residues are all included in the table. Axial stretch is performed in a xyz periodic cell with deformation along to chains, which is the basic attribute of cellulose chains. Simulation for polymer stiffness is a single chain centered in cell. For axial stretch, Poisson effect is presented in CG model and elastic modulus of AA and CG are 133.5 GPa and 130.3 GPa respectively, where reference modulus is 120-140 GPa from experiments^[13;14] and 110-200 GPa from simulations^[16;17;38]. For polymer stiffness, persistence length of AA and CG range from 9.7-9.8 nm and 8.9-10.2 nm, where reference data is 6-25 nm from experiments^[72] and simulation^[73]. We notice it that polymer stiffness simulation is not stable for AA cause cellulose may intertwine with itself in some cases, thus persistence lengths of different length models and average end-to-end distances are also provided. When considering polymer stiffness, joint O atoms between two cellulose residues in AA models and CL1 beads on the backbone in CG models are considered particles. Reference data for training are based on AA information only, and mapped AA trajectories are compared with CG trajectories after training. In this paper, all effective k is smaller than their initial guess based on distributions, especially for angle and dihedral to reproduce polymer stiffness performance in a reduced degree of freedom system (Supplementary Table S1 and Table S2). Compared bonded geometry parameter distributions are enclosed in Supplementary Figure S5.

Table 3: Bonded properties

type		AA	CG	Error
Axial modulus (GPa)		133.5	130.5	2.25%
Persistence length (nm)	10	9.755	8.990	7.84%
	20	9.815	10.176	3.68%
	30	9.716	10.106	4.01%
End-to-end distance (nm)	10	4.523	4.529	0.01%
	20	9.355	9.535	3.52%
	30	13.536	13.536	0.08%

Table 4: Nonbonded properties

type		AA	CG	Error
Strength (MPa)	V	1224.0±9.7	1191.9±6.0	2.62%
	H	638.2±4.8	653.5±1.1	2.40%
	S	467.0±3.7	509.8±4.6	8.99%
Toughness (MPa)	V	111.0±2.5	117.0±3.2	0.54%
	H	77.9±2.8	78.1±1.2	0.26%
	S	190.1±4.6	166.9±3.8	12.20%
Direction angle	R	2.29±0.00	2.33±0.00	1.75%
	F	1.92±0.02	2.02±0.01	5.21%

3.3 Nonbonded properties

Nonbonded properties contains transverse strength, toughness (Table 4 and Figure 7). Transverse stretches are performed in a xyz periodic cell with deformation perpendicular to chains. Reference strengths of vertical, horizontal and slant model are 0.9 GPa^[17], 0.5 GPa^[17] and 0.7

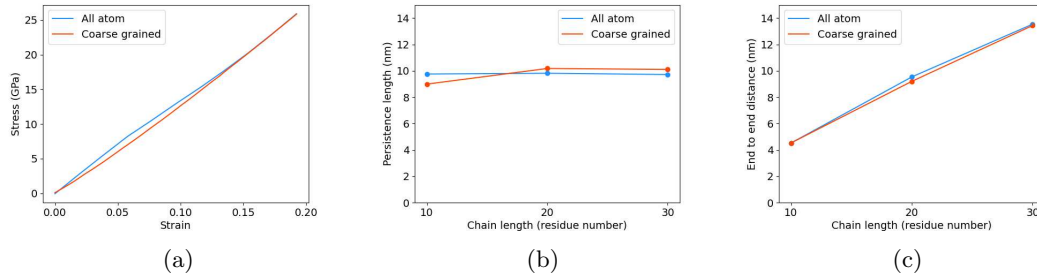


Figure 6: Bonded properties. (a) Axial elastic modulus. The elastic modulus of AA and CG are 133.5 GPa and 130.5 GPa separately, corresponding with each other and reference^[38]. (b)(c) Polymer stiffness containing persistence length and end to end distance. The persistence lengths of AA and CG models of three different length of chains are about 10 nm, and the errors are less than 15% and in agreement with reference^[72]. And the end to end distances of AA and CG models are also quite close with errors less than 5%.

GPa^[38], which are well reproduced by both AA and CG simulations. To reduce the impacts of randomness of simulations, 100 replica of transverse stretch are performed. The distributions of strength and toughness of CG models are close to AA reference data, only the distributions of CG models are narrower than AA counterparts. Average strength and toughness values are quite close to AA data anyway. The frictional sliding for slant models is also reproduced, and this is quantitatively validated by direction angle of slant models (Supplementary Figure S2). These data reveal the validation of this CG model to reproduce transverse anisotropy and frictional sliding. Although all σ is larger than expected, equilibrium distances in CG models are only slightly larger than AA models (less than %15, Table 2). Compared nonbonded equilibrium distance distributions are enclosed in Supplementary Figure S6. Stress-strain curve example (Supplementary Figure S7), radical distribution function, radius of gyration and root mean square deviation (Supplementary Figure S8) are also well reproduced.

3.4 Additional inspection

Additional inspections about the mechanical properties of this CG models are checked as below to check its transferability and generalization in other cases.

3.4.1 Draw-out and Tear-apart

In fracture mechanics, fractures could be classified as three types: opening, in-plane-shear and out-of-plane-shear, and transverse stretch only corresponds to opening fracture. Draw-out (in-plane-shear) and Tear-apart (out-of-plane-shear) are tested by Steered Molecular Dynamics (Figure 8). Draw-out is carried out in a periodic cell with NPT ensemble, and the midst cellulose chain is pulled out of CNC. Tear-apart is to tow the tips of middle part of cellulose chains to move perpendicularly to its backbone, which is in NVT ensemble. Structure and Force-displacement are provided in Figure 8. Determined by periodic structure and hydrogen bonding of cellulose chains, the draw-out is a periodic process with fading of max force with a good agreement of max force and frequency; Tear-apart of both AA and CG model is a force increasing process and their displacement and the max force are close. These results tell us that this CG model could illustrate three type fractures of CNC accurately.

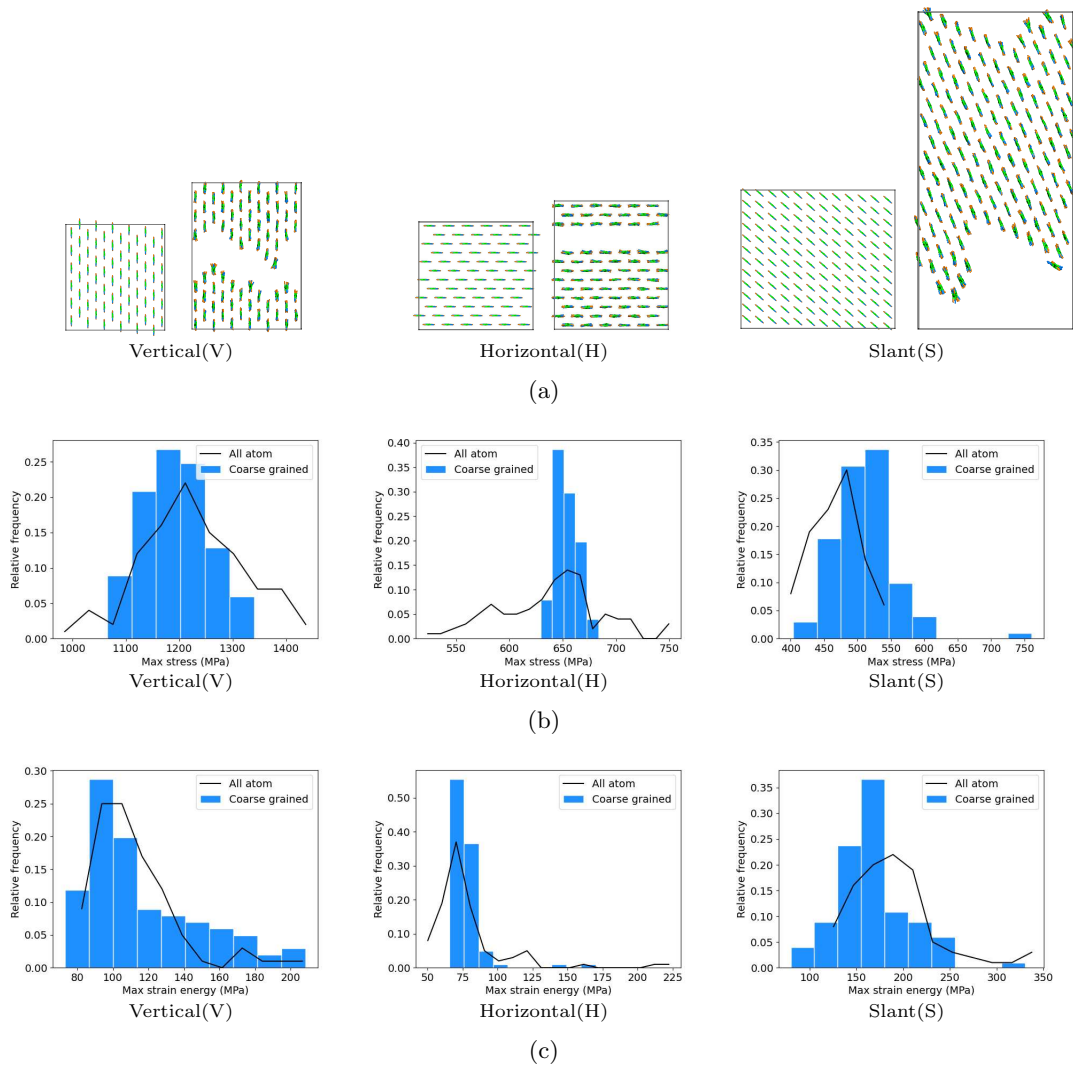


Figure 7: Nonbonded properties. (a) CG model characteristic behaviors. The important frictional sliding in slant direction and fragile fractures in vertical and horizontal directions are reproduced. (b) Strength and (c) toughness distributions of transverse stretches. 100 replica simulations with different random seeds of both AA and CG models in three directions are performed independently. For vertical and slant models, strength and toughness histograms are reproduced consistently as their mean values and standard error are quite close. Despite the accuracy of means values, CG horizontal models provide narrower distributions, which are also within expectation.

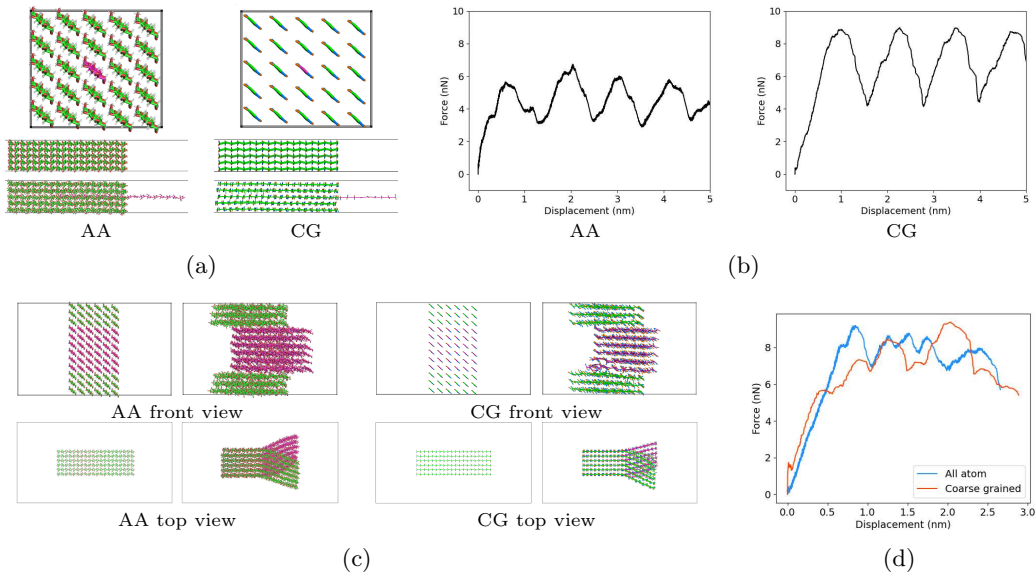


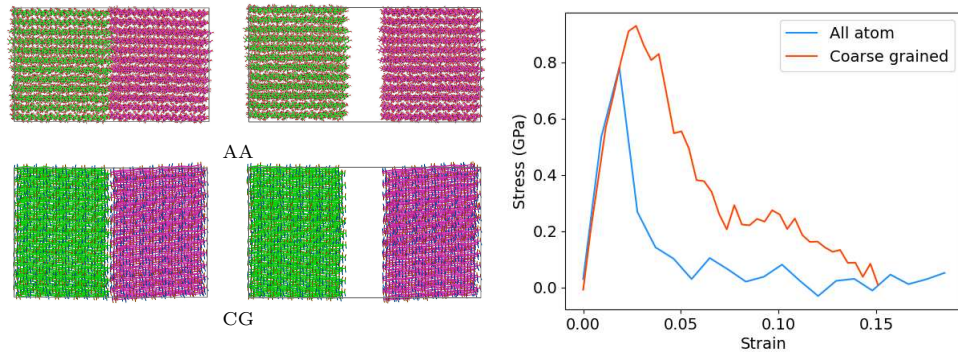
Figure 8: Draw-out (a)(b) and Tear-apart (c)(d). Transverse stretch resembles an opening fracture, while in-plane-shear and out-of-plane shear are examined by Draw-out and Tear-apart simulations. Draw-out and Tear-apart are performed in NPT and NVT ensemble separately by Steered Molecular Dynamics with a axial towing of the midst cellulose chain or perpendicular towing of the middle part. AA and CG simulations for Draw-out all present a periodic fading force curve which are ruled by its structure, whereas the force of Tear-apart is incremental. Max force and frequency of Draw-out of Tear-apart match with each other. Thus this CG model could also represent in-plane-shear and out-of-plane shear of CNC quantitatively.

3.4.2 Adhesion and bending

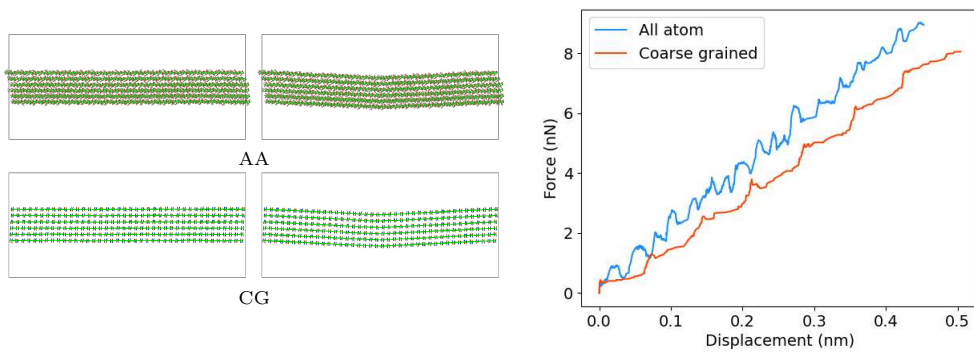
Although our CG models are designed for pure periodic systems, adhesion and bending loads are applied to check its ability in non-periodic systems (Figure 9). Adhesion is performed to check adhesion energy of two nearby non-periodic CNC in the axial direction. Bending is a vertical load at the center point of cellulose bundles which could be seen as a fixed end beam. Adhesion energy of CG model is obviously larger than AA, and the slightly lower force of CG model in Bending may be influenced by bonded force rescales of angles and dihedrals. The results confirm that this CG model could also be used in non-periodic CNC systems but the accuracy is a little bit lower.

3.4.3 Transverse arrangement

Unlike former bonded directionality CG models^[36–39], this CG present directionality by mapping and hydrogen-bond-like interactions. This makes one thing possible: considering transverse arrangement of CNC with different patterns instead of only considering them as a big crystal structure. Two arrangement pattern named cross and symmetric are compared with a large crystal structure, and their fracture and performance differ a lot as the results show Figure 10. The symmetric pattern is inspired by twin structure and the results show that this pattern has a better toughness comparing to crystal. Inter layer friction are impeded and transformed into local rotations, achieving better toughness and ductility in symmetric pattern. Vulnerable lower-upper interfaces of cross pattern are responsible for its lower toughness, but interestingly toughness of cross patterns is not lower than crystal pattern. These results emphasize the importance of transverse arrangement, which are could not be described by former coarse grained



(a)



(b)

Figure 9: Adhesion and Bending in non-periodic systems. (a) Adhesion. In Adhesion, two CNCs are placed tightly close to each other along the chain direction and connected by adhesion energy. Then they are pulled out with each other. Adhesion energy of CG model is obviously larger. (b) Bending. Vertical load is applied at the center of CNC bundle to induce bending. Force curves of Adhesion and Bending confirm the capabilities of this CG model in non-periodic systems. Unlike axial modulus dominated by bonds, bending is also impacted by angles and dihedrals. The slight lower bending modulus may result from the rescale of angle and dihedral force constants as we mentioned before.

models.

3.4.4 Brick-and-mortar

Revealed by former researches, highly aligned CNCs can assemble as different arrangements, such as staggered brick-and-mortar structure^[74;75] and chiral nematic helicoidal structures^[75]. Brick-and-mortar structure could increase stiffness, strength and toughness, and this test could be seen as a CNC level in-plane-shear. In these simulations, 4×8 CNC are assembled and each one is composed of 36 parallel cellulose chains. The elementary cellulose chains are 10, 20, 30 or 40 cellulose residues long. There are already 1.5 million atoms in AA system if the elementary brick is 60 cellulose residues long, and 80 cellulose residues length bricks are only simulated in CG models. Local-slips and small non-local slips appeared as frictional fracture behavior for staggered structures regardless of basic brick length. These results also demonstrate a positive correlation of toughness and the overlapping length.

3.4.5 Computation efficiency

Lower computational cost is the key advantage of coarse grained models. Computation efficiency of this CG model and its AA counterpart are compared by simulation performance reported by simulation software respectively. A series of square periodic CNC (square means row number and column number of cross section of CNC is the same) equilibrium simulations of different sizes are used as benchmarks, in which atom number of AA models is ranged from 7000 to 900000. Cause HB nonbonded interaction do not support GPU acceleration yet, AA simulation using only the same amount of CPU resources are presented Figure 12. For CG simulations and AA simulations with CPU only, 6 cores are occupied exclusive for each task; for AA simulations accelerated by GPU, 6 cores and an additional exclusive GPU are allocated. The results confirm that this CG model could reach 20 times faster than AA models under using same resources and even twice faster than AA models with much more accelerations. When GPU accelerated HB nonbonded interaction is developed and tested, its potential will be fully exploited.

Discussions

Cellulose materials are usually composed of long and thin cellulose nanofibrils and former CG models of cellulose usually lay their stress on axial properties of cellulose^[29;30]. However, CNCs are anisotropic and much shorter, and its transverse properties should be disparaged, which are quite important for future cellulose material design. Some of them present transverse anisotropy by anisotropic particles^[26;35] or additional artificial bonds^[36-39], which are still incapable to present transverse anisotropy of CNC.

The challenge of CG cellulose modelling and the main characteristics of this CG model are the complanate sidechains and hydrogen bonding interactions. And this CG model could reveal frictional sliding and transverse arrangement, which are two critical properties for CNCs transverse anisotropy and former CG models could not reflect accurately. Except for the hydrogen bonding interactions, only harmonic potentials and Lennard-Jones potentials are included for bonded and nonbonded interactions. Our model also confirms the potential parameterization capability of RL: only a discriminant reward function is required. The reward function for RL includes match degree of several mechanical properties: bonded properties (axial modulus, polymer stiffness) and nonbonded properties (transverse strength and toughness), and this resultant model could

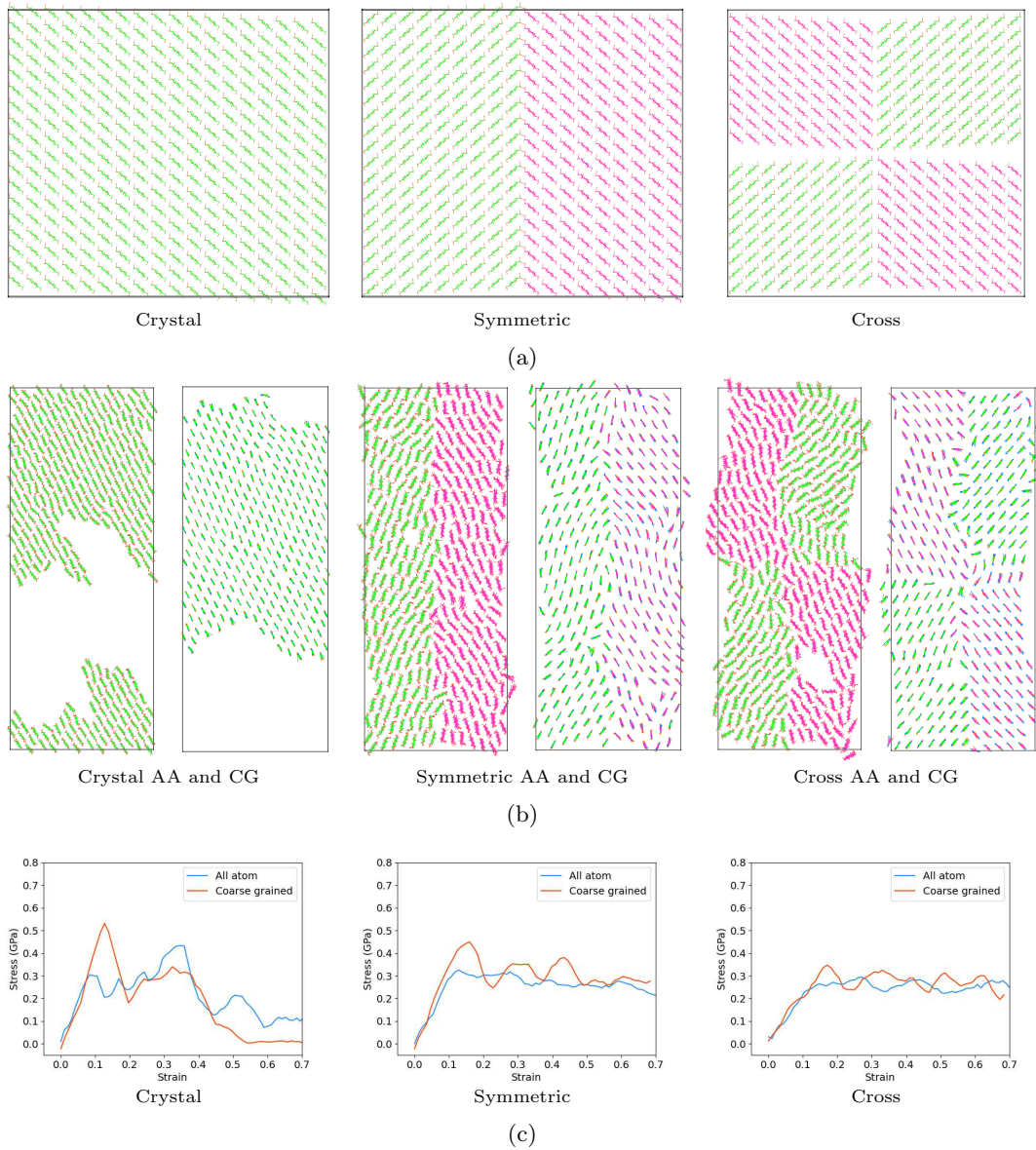


Figure 10: Transverse arrangement. (a) Transverse arrangement patterns. The crystal pattern is as we did for potential parameterization. The symmetric pattern is inspired by twin structure. The cross pattern is a X shape arrangement. (b) Left AA models and right CG models of different arrangement patterns after vertical stretches of same strain. In symmetric pattern and cross pattern, global stretch is composed by deformation of four units whose inter layer frictions are hampered. In this case, local rotations become the dominant behavior and lead a to a better toughness and ductility. (c) Stress-strain curve of three patterns. Transverse arrangements of CNC in symmetric pattern and cross pattern could not be expressed in former CG models of CNC, and should be emphasized more.

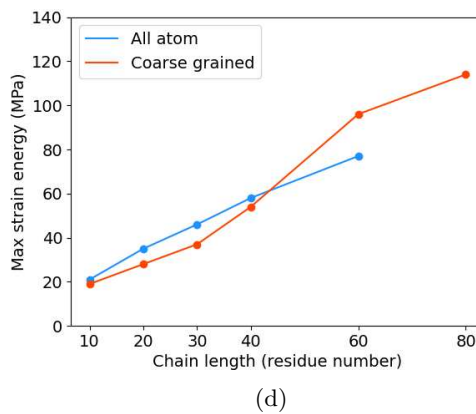
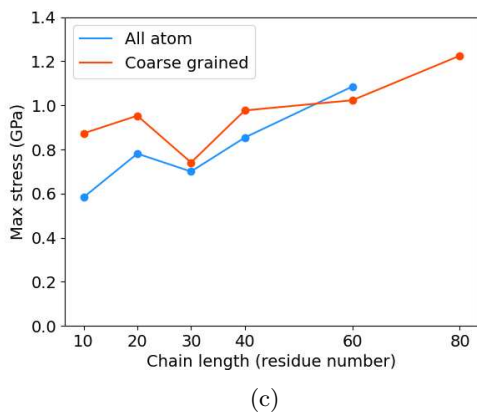


Figure 11: Brick-and-mortar. (a) Brick-and-mortar models and fractures. (b) Stress-strain curve when elementary cellulose chain length is 40 residues. (c) Strength and (d) toughness curve using elementary chain length as variable. Highly aligned CNC could assemble into brick-and-mortar structures^[74;75] in the axial direction and this staggered structure could improve strength and toughness. Brick-and-mortar stretch is also a CNC level in-plane-shear and heavily influenced by length of elementary cellulose chains. This CG model could also describe Brick-and-mortar structure behaviors quantitatively. The fracture of brick-and-mortar is composed of major local slips and non-local small slips, and the toughness correlates positively with the overlapping length.

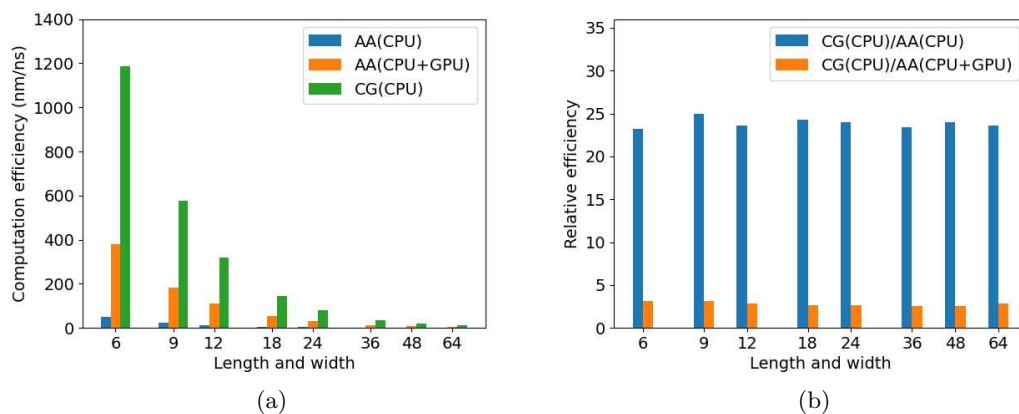


Figure 12: Computation efficiency (a) and (b) relative efficiency with all atom simulation as reference. Currently, HB nonbonded interactions we used does not support GPU acceleration yet. Comparing to AA models with same amount of CPU only resources, this CG model is 20 times faster in CNC equilibrium simulations of different transverse sizes. The efficiency of CG model is still third times of AA model if additional exclusive GPU resources are utilized. Its computation efficiency has not been fully proved yet.

reproduce xyz three dimensional anisotropy and transverse frictional sliding. RL may be much more widely applied for potential parameterization in the future.

However, several problems are also presented in this CG model. The first one is the nonbonded equilibrium distance. Equilibrium distances of this CG model are larger than AA counterpart (Supplementary Figure S6) and the enlargement of CL2-CL3 nonbonded distance coefficients are determined by RL (Figure 5). That means the distance coefficients and equilibrium distances do not correspond to well-relaxed AA equilibrium distances or characteristic points of radial distribution function. Equilibrium distance in this paper is defined as average minimum distance in this paper. Nearly all minimum distances of pairs are from beads of different hydrogen bonding layers, only the minimum distances of CL2-CL3 are from beads in same hydrogen bonding layer. Then we infer that, equilibrium distances from inter layer pairs are appropriate estimations of σ of LJ potential cause dominant nonbonded interaction is hydrogen bonds in a hydrogen bonding layer. And the overall nonbonded distance coefficients enlargement may be influenced by the enlargement of σ_{p23} to retain the crystal structure. Moreover, the enlargement of σ_{p23} may be a unifying of σ cause the equilibrium distance of CL2 and CL3 is also the smallest. Inter layer frictional sliding may be presented more easily if all σ are close with each other.

Angle and dihedral interaction force constants are also obvious problems. CG model with a much lower degree of freedom has to compensate poly stiffness by lowering force constants (Supplementary Table S2). Former CG model addressing persistence length does not require a precious match (40 nm compared to 10 nm)^[34], or they choose to estimate the persistence length of a bundle of cellulose chains^[76] instead of one free chain. For other properties involving angle and dihedral like the bending, smaller force constants may cause problems like the lower stress of Bending.

Others smaller problems also exist. Our model may not perform well in non-periodic cellulose systems such as the Adhesion simulation; the pressure curve of CG model in NPT ensemble has a larger oscillation amplitude. And some molecular details are ignored in this CG model. For instance, the rotational degree of freedom from hydrogen atoms on side chain hydroxyls is neglected in harmonic potentials (Supplementary Figure S9). Moreover, one technical problem also restrains the application potential of this CG model: the hydrogen-bond-like interaction we use does not support GPU acceleration temporarily and the computation efficiency of this CG model has not been fully released yet.

Anyway, as the early birds to introduce hydrogen bonds into CG models of CNC, this CG model may also help future researches. The development of cellulose CG models is mainly focusing on native cellulose. However, solvent environments especially humidity are key factors of cellulose materials^[34;77-79] and not well presented in CG cellulose models^[30]. Chemical surface modifications, and interaction with other molecules like hemicellulose or lignin, are also critical for performance enhancement of cellulose materials. All of these problems are tightly connected to the side chain hydroxyls of cellulose. Lack in resources and expertise about these interactions, we do not consider interaction with other molecules in this CG model. With the help of hydrogen-bond-like interactions, later CG model could try to present more complex properties of cellulose. We wish this model could help a little for future CG cellulose models.

As an application of RL for potential parameterization, our methods and implementations are not heavily dependent on cellulose and may help later CG model development. And transfer Learning and Imitation Learning may be applied to further accelerate potential parameterization by RL in the future.

Conclusions

In this paper, we introduce a novel cellulose coarse grained model with explicit complanate sidechain beads and hydrogen-bond-like interactions that is able to reproduce transverse frictional sliding and anisotropic mechanical properties of cellulose nanocrystals. Without usage of anisotropic particles or additional bonds, strength and toughness in three characteristic directions of orthotropic cross section are quantitatively reproduced. We are early birds to apply degenerate Reinforcement Learning as a nonlinear optimizer to do direct analytical potential parameterization, and its physical meanings are enhanced by integration of Boltzmann inversion. This model is a eclecticism of physical knowledge, traditional modeling and machine learning methods, and helpful to understand the importance of hydrogen bonds and anisotropy of cellulose nanocrystals. Our results confirm that, with an appropriate reward function based on target properties and statistics-guided reduction, Reinforcement Learning agent could determine proper coefficients under the guidance of reward function without consuming a large amount of computational resources. The target anisotropic properties we take into account include two parts: axial elastic modulus and polymer stiffness; transverse stretch strength and toughness, which are all closely matched with errors below %15. Transferability and generalization of this coarse grained model are proved by several successful additional inspections including in-plane-shear, out-of-plane-shear, adhesion energy, bending, transverse arrangement and brick-and-mortar structure. Transverse anisotropy which is not well presented quantitatively in CG models before, is quite important for transverse arrangement. Two transverse arrangement patterns with better toughness and ductile than crystal are. And we find a positive correlation between overlapping length and toughness of brick-and-mortar structure. The data of transverse arrangement and brick-and-mortar structure may be helpful to advanced material design in the future. This model with may also help to address interactions of cellulose and polar molecules like water in coarse grained level. This work emphasizes that, machine learning methods could also be utilized to construct effective analytical potentials which is better in explainability, transferability and kinetics. Although our results prove the efficiency of Reinforcement Learning, many refinements are still remained to be explored especially in the field of molecule researches. For example, the necessity of inspiration of human knowledge and traditional methods like Boltzmann inversion is still in question. Finally, our parameterization approach is agnostic to the application case, which means our procedures are also applicable to other molecule systems. Transfer Learning and Imitation Learning could also be integrated with RL to solve similar problems in the future.

References

- [1] Robert J Moon, Gregory T Schueneman, and John Simonsen. Overview of cellulose nanomaterials, their capabilities and applications. *Jom*, 68:2383–2394, 2016.
- [2] Joo-Hyung Kim, Bong Sup Shim, Heung Soo Kim, Young-Jun Lee, Seung-Ki Min, Daseul Jang, Zafar Abas, and Jaehwan Kim. Review of nanocellulose for sustainable future materials. *International Journal of Precision Engineering and Manufacturing-Green Technology*, 2:197–213, 2015.
- [3] Hwee Li Teo and Roswanira Abdul Wahab. Towards an eco-friendly deconstruction of agro-industrial biomass and preparation of renewable cellulose nanomaterials: A review. *International journal of biological macromolecules*, 161:1414–1430, 2020.
- [4] Robert J Moon, Ashlie Martini, John Nairn, John Simonsen, and Jeff Youngblood. Cellulose nanomaterials review: structure, properties and nanocomposites. *Chemical Society Reviews*, 40(7):3941–3994, 2011.
- [5] Qianqian Zhu, Simeng Liu, Jianzhong Sun, Jun Liu, C Joseph Kirubaharan, Honglei Chen, Weihua Xu, and Qianqian Wang. Stimuli-responsive cellulose nanomaterials for smart applications. *Carbohydrate Polymers*, 235:115933, 2020.

- [6] Haishun Du, Wei Liu, Miaomiao Zhang, Chuanling Si, Xinyu Zhang, and Bin Li. Cellulose nanocrystals and cellulose nanofibrils based hydrogels for biomedical applications. *Carbohydrate polymers*, 209:130–144, 2019.
- [7] Jiwoo Yu, Aurelia C Wang, Mingyue Zhang, and Zhiqun Lin. Water treatment via non-membrane inorganic nanoparticles/cellulose composites. *Materials Today*, 50:329–357, 2021.
- [8] Huayu Liu, Haishun Du, Ting Zheng, Kun Liu, Xingxiang Ji, Ting Xu, Xinyu Zhang, and Chuanling Si. Cellulose based composite foams and aerogels for advanced energy storage devices. *Chemical Engineering Journal*, 426:130817, 2021.
- [9] Yang Wang, Lina Zhang, Jinping Zhou, and Ang Lu. Flexible and transparent cellulose-based ionic film as a humidity sensor. *ACS applied materials & interfaces*, 12(6):7631–7638, 2020.
- [10] Davi Texeira Reis, Igor Hernandez Santos Ribeiro, and Douglas Henrique Pereira. Dft study of the application of polymers cellulose and cellulose acetate for adsorption of metal ions (cd 2+, cu 2+ and cr 3+) potentially toxic. *Polymer Bulletin*, 77:3443–3456, 2020.
- [11] Chuantao Zhu, Susanna Monti, and Aji P Mathew. Evaluation of nanocellulose interaction with water pollutants using nanocellulose colloidal probes and molecular dynamic simulations. *Carbohydrate polymers*, 229:115510, 2020.
- [12] Pan Chen, Yu Ogawa, Yoshiharu Nishiyama, Ahmed E Ismail, and Karim Mazeau. Linear, non-linear and plastic bending deformation of cellulose nanocrystals. *Physical Chemistry Chemical Physics*, 18(29):19880–19887, 2016.
- [13] Imke Diddens, Bridget Murphy, Michael Krisch, and Martin Muller. Anisotropic elastic properties of cellulose measured using inelastic x-ray scattering. *Macromolecules*, 41(24):9755–9759, 2008.
- [14] Shinichiro Iwamoto, Weihua Kai, Akira Isogai, and Tadahisa Iwata. Elastic modulus of single cellulose microfibrils from tunicate measured by atomic force microscopy. *Biomacromolecules*, 10(9):2571–2576, 2009.
- [15] Ryan Wagner, Robert J Moon, and Arvind Raman. Mechanical properties of cellulose nanomaterials studied by contact resonance atomic force microscopy. *Cellulose*, 23:1031–1041, 2016.
- [16] Fernando L Dri, Louis G Hector, Robert J Moon, and Pablo D Zavattieri. Anisotropy of the elastic properties of crystalline cellulose β from first principles density functional theory with van der waals interactions. *Cellulose*, 20:2703–2718, 2013.
- [17] Xiawa Wu, Robert J Moon, and Ashlie Martini. Tensile strength of β crystalline cellulose predicted by molecular dynamics simulation. *Cellulose*, 21:2233–2245, 2014.
- [18] Qinghua Meng, Bo Li, Teng Li, and Xi-Qiao Feng. Effects of nanofiber orientations on the fracture toughness of cellulose nanopaper. *Engineering Fracture Mechanics*, 194:350–361, 2018.
- [19] Qinghua Meng, Bo Li, Teng Li, and Xi-Qiao Feng. A multiscale crack-bridging model of cellulose nanopaper. *Journal of the Mechanics and Physics of Solids*, 103:22–39, 2017.
- [20] Tongye Shen and S Gnanakaran. The stability of cellulose: a statistical perspective from a coarse-grained model of hydrogen-bond networks. *Biophysical journal*, 96(8):3032–3040, 2009.
- [21] Cyrus Djahedi, Malin Bergenstråhle-Wohlert, Lars A Berglund, and Jakob Wohlert. Role of hydrogen bonding in cellulose deformation: the leverage effect analyzed by molecular modeling. *Cellulose*, 23:2315–2323, 2016.
- [22] Malin Wohlert, Tobias Benselfelt, Lars Wågberg, István Furó, Lars A Berglund, and Jakob Wohlert. Cellulose and the role of hydrogen bonds: not in charge of everything. *Cellulose*, pages 1–23, 2022.
- [23] Xiawa Wu, Robert J Moon, and Ashlie Martini. Atomistic simulation of frictional sliding between cellulose β nanocrystals. *Tribology Letters*, 52:395–405, 2013.
- [24] Chi Zhang, Sinan Ketten, Dominique Derome, and Jan Carmeliet. Hydrogen bonds dominated frictional stick-slip of cellulose nanocrystals. *Carbohydrate Polymers*, 258:117682, 2021.
- [25] Aleksandar Y Mehandzhiyski and Igor Zozoulenko. A review of cellulose coarse-grained models and their applications. *Polysaccharides*, 2(2):257–270, 2021.

- [26] Nicolas Rolland, Aleksandar Y Mehandzhiyski, Mohit Garg, Mathieu Linares, and Igor V Zozoulenko. New patchy particle model with anisotropic patches for molecular dynamics simulations: Application to a coarse-grained model of cellulose nanocrystal. *Journal of chemical theory and computation*, 16(6):3699–3711, 2020.
- [27] Aleksandar Y Mehandzhiyski, Nicolas Rolland, Mohit Garg, Jakob Wohlert, Mathieu Linares, and Igor Zozoulenko. A novel supra coarse-grained model for cellulose. *Cellulose*, 27:4221–4234, 2020.
- [28] Zhaofan Li and Wenjie Xia. Coarse-grained modeling of nanocellulose network towards understanding the mechanical performance. *Extreme Mechanics Letters*, 40:100942, 2020.
- [29] Xin Qin, Shizhe Feng, Zhaoxu Meng, and Sinan Keten. Optimizing the mechanical properties of cellulose nanopaper through surface energy and critical length scale considerations. *Cellulose*, 24:3289–3299, 2017.
- [30] Upamanyu Ray, Zhenqian Pang, and Teng Li. Mechanics of cellulose nanopaper using a scalable coarse-grained modeling scheme. *Cellulose*, 28(6):3359–3372, 2021.
- [31] Cesar A Lopez, Giovanni Bellesia, Antonio Redondo, Paul Langan, Shishir PS Chundawat, Bruce E Dale, Siewert J Marrink, and S Gnanakaran. Martini coarse-grained model for crystalline cellulose microfibrils. *The Journal of Physical Chemistry B*, 119(2):465–473, 2015.
- [32] Lintao Bu, Gregg T Beckham, Michael F Crowley, Christopher H Chang, James F Matthews, Yannick J Bomble, William S Adney, Michael E Himmel, and Mark R Nimlos. The energy landscape for the interaction of the family 1 carbohydrate-binding module and the cellulose surface is altered by hydrolyzed glycosidic bonds. *The Journal of Physical Chemistry B*, 113(31):10994–11002, 2009.
- [33] Jakob Wohlert and Lars A Berglund. A coarse-grained model for molecular dynamics simulations of native cellulose. *Journal of Chemical Theory and Computation*, 7(3):753–760, 2011.
- [34] Srinivas Goundla, Cheng Xiaolin, et al. Coarse-grain model for natural cellulose fibrils in explicit water. 2014.
- [35] Huong TL Nguyen and David M Huang. Systematic bottom-up molecular coarse-graining via force and torque matching using anisotropic particles. *The Journal of Chemical Physics*, 156(18), 2022.
- [36] Bingxin Fan and Janna K Maranas. Coarse-grained simulation of cellulose $i\beta$ with application to long fibrils. *Cellulose*, 22:31–44, 2015.
- [37] Majid G Ramezani and Behnoush Golchinfar. Mechanical properties of cellulose nanocrystal (cnc) bundles: Coarse-grained molecular dynamic simulation. *Journal of Composites Science*, 3(2):57, 2019.
- [38] Mehdi Shishehbor and Pablo D Zavattieri. Effects of interface properties on the mechanical properties of bio-inspired cellulose nanocrystal (cnc)-based materials. *Journal of the Mechanics and Physics of Solids*, 124:871–896, 2019.
- [39] Mehdi Shishehbor, Hyeyoung Son, Md Nuruddin, Jeffrey P Youngblood, Chelsea Davis, and Pablo D Zavattieri. Influence of alignment and microstructure features on the mechanical properties and failure mechanisms of cellulose nanocrystals (cnc) films. *Journal of the Mechanical Behavior of Biomedical Materials*, 118:104399, 2021.
- [40] Frank Noé, Alexandre Tkatchenko, Klaus-Robert Müller, and Cecilia Clementi. Machine learning for molecular simulation. *Annual review of physical chemistry*, 71(1):361–390, 2020.
- [41] Raidel Martin-Barrios, Edisel Navas-Conyedo, Xuyi Zhang, Yunwei Chen, and Jorge Gulín-González. An overview about neural networks potentials in molecular dynamics simulation. *International Journal of Quantum Chemistry*, 124(11):e27389, 2024.
- [42] Wojciech Samek, Grégoire Montavon, Sebastian Lapuschkin, Christopher J Anders, and Klaus-Robert Müller. Explaining deep neural networks and beyond: A review of methods and applications. *Proceedings of the IEEE*, 109(3):247–278, 2021.
- [43] Rohit Batra and Subramanian Sankaranarayanan. Machine learning for multi-fidelity scale bridging and dynamical simulations of materials. *Journal of Physics: Materials*, 3(3):031002, 2020.
- [44] Bridgette J Befort, Ryan S DeFever, Garrett M Tow, Alexander W Dowling, and Edward J Maginn. Machine learning directed optimization of classical molecular modeling force fields. *Journal of Chemical Information and Modeling*, 61(9):4400–4414, 2021.

- [45] Jesse M Sestito, Mary L Thatcher, Leshi Shu, Tequila AL Harris, and Yan Wang. Coarse-grained force field calibration based on multiobjective bayesian optimization to simulate water diffusion in poly- ϵ -caprolactone. *The Journal of Physical Chemistry A*, 124(24):5042–5052, 2020.
- [46] Ke Duan, Yonglyu He, Yijun Li, Jiahuan Liu, Junjie Zhang, Yujin Hu, Rongming Lin, Xuelin Wang, Weiming Deng, and Li Li. Machine-learning assisted coarse-grained model for epoxies over wide ranges of temperatures and cross-linking degrees. *Materials and Design*, 183, 2019.
- [47] Henry Chan, Mathew J Cherukara, Badri Narayanan, Troy D Loeffler, Chris Benmore, Stephen K Gray, and Subramanian KRS Sankaranarayanan. Machine learning coarse grained models for water. *Nature communications*, 10(1):379, 2019.
- [48] M Razi, A Narayan, RM Kirby, and D Bedrov. Force-field coefficient optimization of coarse-grained molecular dynamics models with a small computational budget. *Computational Materials Science*, 176:109518, 2020.
- [49] Anirban Chandra, Troy Loeffler, Henry Chan, Xiaoyu Wang, GB Stephenson, Michael J Servis, and Subramanian KRS Sankaranarayanan. Reinforcement learning based hybrid bond-order coarse-grained interatomic potentials for exploring mesoscale aggregation in liquid–liquid mixtures. *The Journal of Chemical Physics*, 159(2), 2023.
- [50] Shenghao Wu, Tianyi Liu, Zhirui Wang, Wen Yan, and Yingxiang Yang. Rlqg: When reinforcement learning meets coarse graining. In *NeurIPS 2022 AI for Science: Progress and Promises*, 2022.
- [51] Sukriti Manna, Troy D Loeffler, Rohit Batra, Suvo Banik, Henry Chan, Bilvin Varughese, Kiran Sasikumar, Michael Sternberg, Tom Peterka, Mathew J Cherukara, et al. Learning in continuous action space for developing high dimensional potential energy models. *Nature communications*, 13(1):368, 2022.
- [52] Benjamin Recht. A tour of reinforcement learning: The view from continuous control. *Annual Review of Control, Robotics, and Autonomous Systems*, 2(1):253–279, 2019.
- [53] Xuhan Liu, Jun Zhang, Zhonghuai Hou, Yi Isaac Yang, and Yi Qin Gao. From predicting to decision making: Reinforcement learning in biomedicine. *Wiley Interdisciplinary Reviews: Computational Molecular Science*, 14(4):e1723, 2024.
- [54] Aidan P Thompson, H Metin Aktulga, Richard Berger, Dan S Bolintineanu, W Michael Brown, Paul S Crozier, Pieter J In’t Veld, Axel Kohlmeyer, Stan G Moore, Trung Dac Nguyen, et al. Lammmps-a flexible simulation tool for particle-based materials modeling at the atomic, meso, and continuum scales. *Computer physics communications*, 271:108171, 2022.
- [55] Stephen L Mayo, Barry D Olafson, and William A Goddard. Dreiding: a generic force field for molecular simulations. *Journal of Physical chemistry*, 94(26):8897–8909, 1990.
- [56] Sakib Matin, Alice EA Allen, Justin Smith, Nicholas Lubbers, Ryan B Jadrich, Richard Messerly, Benjamin Nebgen, Ying Wai Li, Sergei Tretiak, and Kipton Barros. Machine learning potentials with the iterative boltzmann inversion: training to experiment. *Journal of Chemical Theory and Computation*, 20(3):1274–1281, 2024.
- [57] Aditi Khot and Brett M Savoie. δ -learning applied to coarse-grained homogeneous liquids. *The Journal of Chemical Physics*, 159(5), 2023.
- [58] Wujie Wang, Zhenghao Wu, Johannes CB Dietschreit, and Rafael Gómez-Bombarelli. Learning pair potentials using differentiable simulations. *The Journal of Chemical Physics*, 158(4), 2023.
- [59] Valentina Tozzini, Joanna Trylska, Chia-en Chang, and J Andrew McCammon. Flap opening dynamics in hiv-1 protease explored with a coarse-grained model. *Journal of structural biology*, 157(3):606–615, 2007.
- [60] Victor Ruhle, Christoph Junghans, Alexander Lukyanov, Kurt Kremer, and Denis Andrienko. Versatile object-oriented toolkit for coarse-graining applications. *Journal of chemical theory and computation*, 5(12):3211–3223, 2009.
- [61] Jonathan Viquerat, Jean Rabault, Alexander Kuhnle, Hassan Ghraieb, Aurélien Larcher, and Elie Hachem. Direct shape optimization through deep reinforcement learning. *Journal of Computational Physics*, 428:110080, 2021.

- [62] Tuomas Haarnoja, Aurick Zhou, Pieter Abbeel, and Sergey Levine. Soft actor-critic: Off-policy maximum entropy deep reinforcement learning with a stochastic actor. In *International conference on machine learning*, pages 1861–1870. Pmlr, 2018.
- [63] Antonin Raffin, Ashley Hill, Adam Gleave, Anssi Kanervisto, Maximilian Ernestus, and Noah Dormann. Stable-baselines3: Reliable reinforcement learning implementations. *Journal of Machine Learning Research*, 22(268):1–8, 2021.
- [64] Noam Razin, Zixuan Wang, Hubert Strauss, Stanley Wei, Jason D Lee, and Sanjeev Arora. What makes a reward model a good teacher? an optimization perspective. *arXiv preprint arXiv:2503.15477*, 2025.
- [65] Mark James Abraham, Teemu Murtola, Roland Schulz, Szilárd Páll, Jeremy C Smith, Berk Hess, and Erik Lindahl. Gromacs: High performance molecular simulations through multi-level parallelism from laptops to supercomputers. *SoftwareX*, 1:19–25, 2015.
- [66] Par Bjelkmar, Per Larsson, Michel A Cuendet, Berk Hess, and Erik Lindahl. Implementation of the charmm force field in gromacs: analysis of protein stability effects from correction maps, virtual interaction sites, and water models. *Journal of chemical theory and computation*, 6(2):459–466, 2010.
- [67] Jing Huang and Alexander D MacKerell Jr. Charmm36 all-atom additive protein force field: Validation based on comparison to nmr data. *Journal of computational chemistry*, 34(25):2135–2145, 2013.
- [68] Jing Huang, Sarah Rauscher, Grzegorz Nawrocki, Ting Ran, Michael Feig, Bert L De Groot, Helmut Grubmüller, and Alexander D MacKerell Jr. Charmm36m: an improved force field for folded and intrinsically disordered proteins. *Nature methods*, 14(1):71–73, 2017.
- [69] Sunhwan Jo, Taehoon Kim, Vidyashankara G Iyer, and Wonpil Im. Charmm-gui: a web-based graphical user interface for charmm. *Journal of computational chemistry*, 29(11):1859–1865, 2008.
- [70] Jumin Lee, Xi Cheng, Sunhwan Jo, Alexander D MacKerell, Jeffery B Klauda, and Wonpil Im. Charmm-gui input generator for namd, gromacs, amber, openmm, and charmm/openmm simulations using the charmm36 additive force field. *Biophysical journal*, 110(3):641a, 2016.
- [71] Robert Sinko, Shawn Mishra, Luis Ruiz, Nick Brandis, and Sinan Keten. Dimensions of biological cellulose nanocrystals maximize fracture strength. *ACS macro letters*, 3(1):64–69, 2014.
- [72] Mark A Hilton, Harris W Manning, Ireneusz Górniak, Sonia K Brady, Madeline M Johnson, Jochen Zimmer, and Matthew J Lang. Single-molecule investigations of single-chain cellulose biosynthesis. *Proceedings of the National Academy of Sciences*, 119(40):e2122770119, 2022.
- [73] Loes MJ Kroon-Batenburg, Peter H Kruiskamp, Johannes FG Vliegthart, and Jan Kroon. Estimation of the persistence length of polymers by md simulations on small fragments in solution. application to cellulose. *The Journal of Physical Chemistry B*, 101(42):8454–8459, 1997.
- [74] Xiaodong Li, Wei-Che Chang, Yuh J Chao, Rizhi Wang, and Ming Chang. Nanoscale structural and mechanical characterization of a natural nanocomposite material: the shell of red abalone. *Nano letters*, 4(4):613–617, 2004.
- [75] Bharath Natarajan and Jeffrey W Gilman. Bioinspired bouligand cellulose nanocrystal composites: a review of mechanical properties. *Philosophical Transactions of the Royal Society A: Mathematical, Physical and Engineering Sciences*, 376(2112):20170050, 2018.
- [76] Dennis C Glass, Kei Moritsugu, Xiaolin Cheng, and Jeremy C Smith. Reach coarse-grained simulation of a cellulose fiber. *Biomacromolecules*, 13(9):2634–2644, 2012.
- [77] Loukas Petridis, Hugh M O’Neill, Mariah Johnsen, Bingxin Fan, Roland Schulz, Eugene Mamontov, Janna Maranas, Paul Langan, and Jeremy C Smith. Hydration control of the mechanical and dynamical properties of cellulose. *Biomacromolecules*, 15(11):4152–4159, 2014.
- [78] YuanZhen Hou, Qing-Fang Guan, Jun Xia, Zhang-Chi Ling, ZeZhou He, Zi-Meng Han, Huai-Bin Yang, Ping Gu, YinBo Zhu, Shu-Hong Yu, et al. Strengthening and toughening hierarchical nanocellulose via humidity-mediated interface. *ACS nano*, 15(1):1310–1320, 2020.
- [79] Yuanyuan Guo, Wei Wang, and Xuewei Jiang. Molecular dynamics study on mechanical properties of cellulose with water molecules diffusion behavior at different oxygen concentrations. *Forests*, 14(2):371, 2023.

Supplementary information

Following contents are included in the separate Supplementary information.

Figure S1 Figure S2 Figure S3 Figure S4 Figure S5 Figure S6 Figure S7 Figure S8 Figure S9

Table S1 Table S2

Analytical coarse grained potential parameterization by Reinforcement Learning for anisotropic cellulose

Don Xu

keywords: Reinforcement Learning, Boltzmann inversion, coarse grained,
cellulose, anisotropy, hydrogen bond

Supplementary information

Force and energy curve of HB and LJ potentials

Defined with different Lennard-Jones style functions, LJ potential we used applies an energy shift and force smooth to ensure both energy and force reaches zeros at the cutoff distance; HB potential is influenced by the A:H-D angle. Graphical force and energy curves of HB and LJ potentials are displayed in Figure S1 with $\epsilon = 1$ and $\sigma = 1$ for both.

Transverse stretch performance at different stretch speed

For slant models, frictional sliding is quantitatively by direction angle defined as projection angle of vectors by two carbon atoms (Figure S2). Before choosing 10.0 nm/ns as the stretch speed for potential parameterization, transverse stretch performances in three characteristic directions and their standard error at 0.1, 1.0, 2.0, 4.0, 10.0, 20.0 and 40.0 nm/ns are checked (Figure S3). Except for 0.1 nm/ns (at which speed 10 replica simulations are executed to save resources), 100 replica transverse stretches performance data are collected. These results confirm that stretch speed is not the critical factor for transverse performances and nearly all performance deviations at other speed are less than 15% based on average data at 10.0 nm/ns. Only the toughness data of vertical model at 40.0 nm/ns is beyond 15% and 10.0 nm/ns is chosen. Stress-strain curves with max stress distribution and Strain energy curve with max strain energy distribution at 10.0 nm/ns are also provided at Figure S4.

Bonded properties without rescale

In this paper, all bonded force constants are rescaled to be smaller than their initial guesses by Boltzmann inversion (Table S1). Bonded properties corresponding to unrescaled bonded force constants are introduced in Table S2, in which persistence length data are not acceptable. The degree of freedom of CG models are obviously smaller than their AA models, and we assume that smaller bonded force constants for angles and dihedrals are critical to reproduce polymer stiffness.

Comparison of bonded geometry parameter distributions

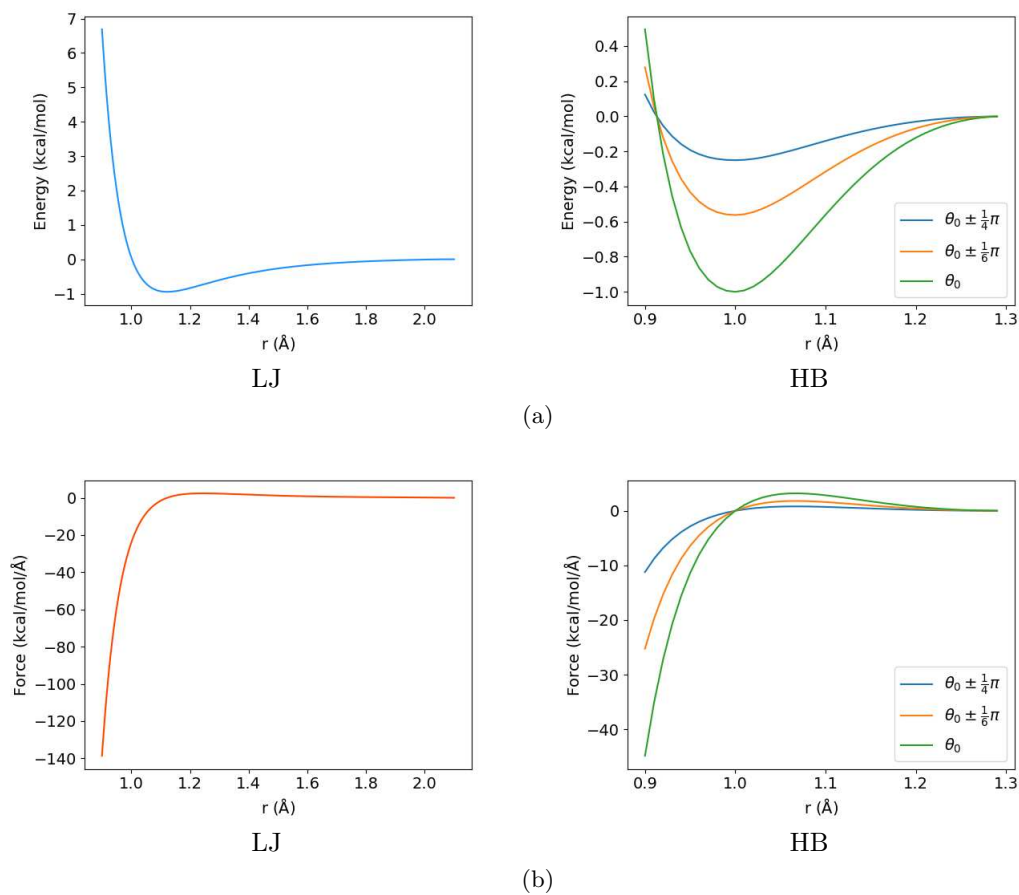


Figure S1: Nonbonded energy and force curves. (a) LJ and HB energy curves. (b) LJ and HB force curves. Both LJ and HB potential are based on Lennard-Jones interactions and they follow 12-6 formula and 12-10 formula respectively. The key difference is that HB potential is scaled by the power of cosine of A:H-D angle meanwhile energy shift and force smooth of LJ potential confirm zero energy and force at the cutoff distance. These curves are defined using $\epsilon = 1$ and $\sigma = 1$.

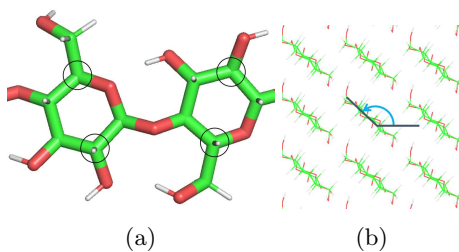


Figure S2: Direction angle definition. (a) The considered carbon atoms for direction angle. (b) The projection angle of consider carbon atoms is defined as the direction angle. Direction angle is defined to quantify frictional sliding of slant models.

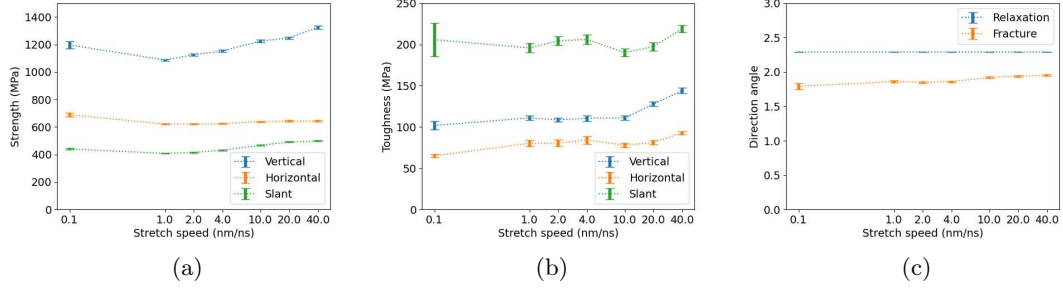


Figure S3: AA transverse stretch performance with speed. Transverse (a) strength, (b) toughness and (c) direction angle with standard error at different stretch speeds are presented. 100 replica transverse stretches at 1.0, 2.0, 4.0, 10.0, 20.0 and 40.0 nm/ns are summarized with average and standard error. Only 10 replica at 0.1 nm/ns are enforced to control computation costs. All data except for toughness of vertical models at 40.0 nm/ns are within 15% relative deviations referenced to average values at 10.0 nm/ns. 10.0 nm/ns is chosen for parameterization finally.

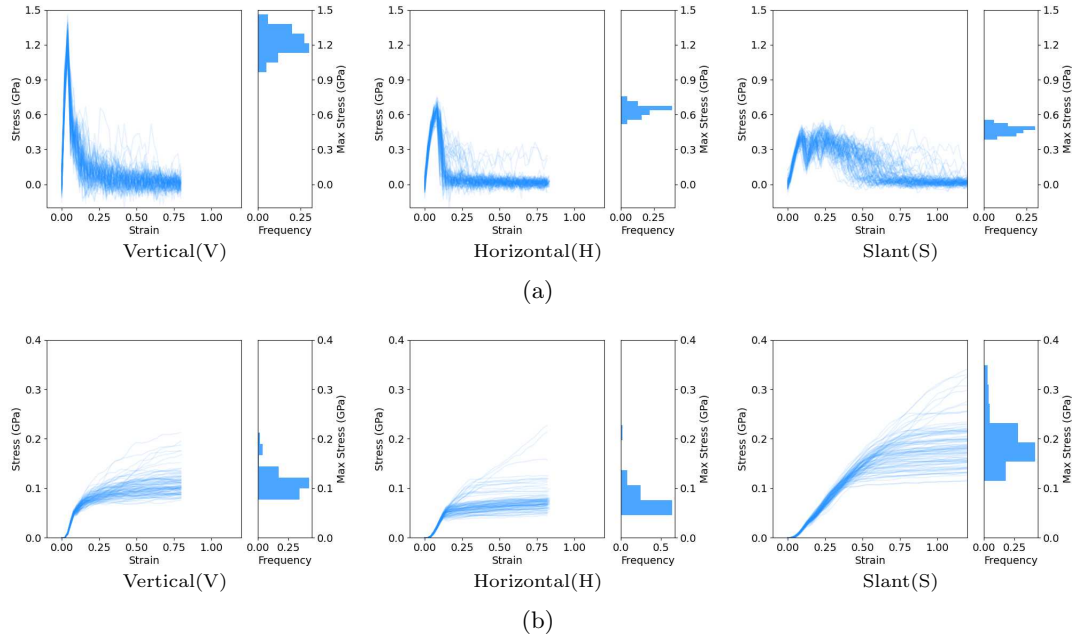


Figure S4: AA transverse stretch (a) stress-strain and (b) strain energy collections in characteristic directions at 10.0 nm/ns. Each collection contains 100 curves, and strength or toughness distribution is enclosed on the right.

Table S1: Bonded force constants without rescale

type	id	Optimized	Unrescaled
$k(\text{kcal/mol}/\text{\AA}^2)$			
bond	1	64.06	110.3
	2	82.42	141.9
	3	112.3	193.3
$k(\text{kcal/mol})$			
angle	1	30.97	274.5
	2	38.79	343.7
	3	30.52	270.5
	4	27.28	241.8
	5	25.97	230.2
	6	22.42	198.7
$k(\text{kcal/mol})$			
improper	1	0.1702	21.57
	2	0.1555	19.71
	3	0.1698	21.53

Table S2: Bonded properties without rescale

type		AA	CG	Error
Axial modulus (GPa)		133.5	233.8	75.13%
Persistence length (nm)	10	9.755	306.1	3137.87%
	20	9.815	310.5	3063.53%
	30	9.716	298.6	2973.33%
End-to-end distance (nm)	10	4.523	4.689	3.67%
	20	9.355	9.888	5.70%
	30	13.536	15.069	11.33%

After parameterization, bonded geometry parameters are sampled from slant CNC equilibrium simulations by CG models with reference data from mapped AA modelsFigure S5. The bonded geometry parameters of CG models are quite close to AA reference but larger dispersions are caused by smaller bonded force constants.

Comparison of nonbonded equilibrium distance distributions

After parameterization, nonbonded equilibrium distances are sampled from slant CNC equilibrium simulations by CG models with reference data from mapped AA modelsFigure S6. As we mentioned in Results-Coefficients part, nonbonded distance coefficients are usually larger than the estimated range $[0.89d^e, 1.00d^e]$ after parameterization by RL. These deviations of equilibrium distances are acceptable anyway.

Comparison of transverse stress-strain examples and structure properties

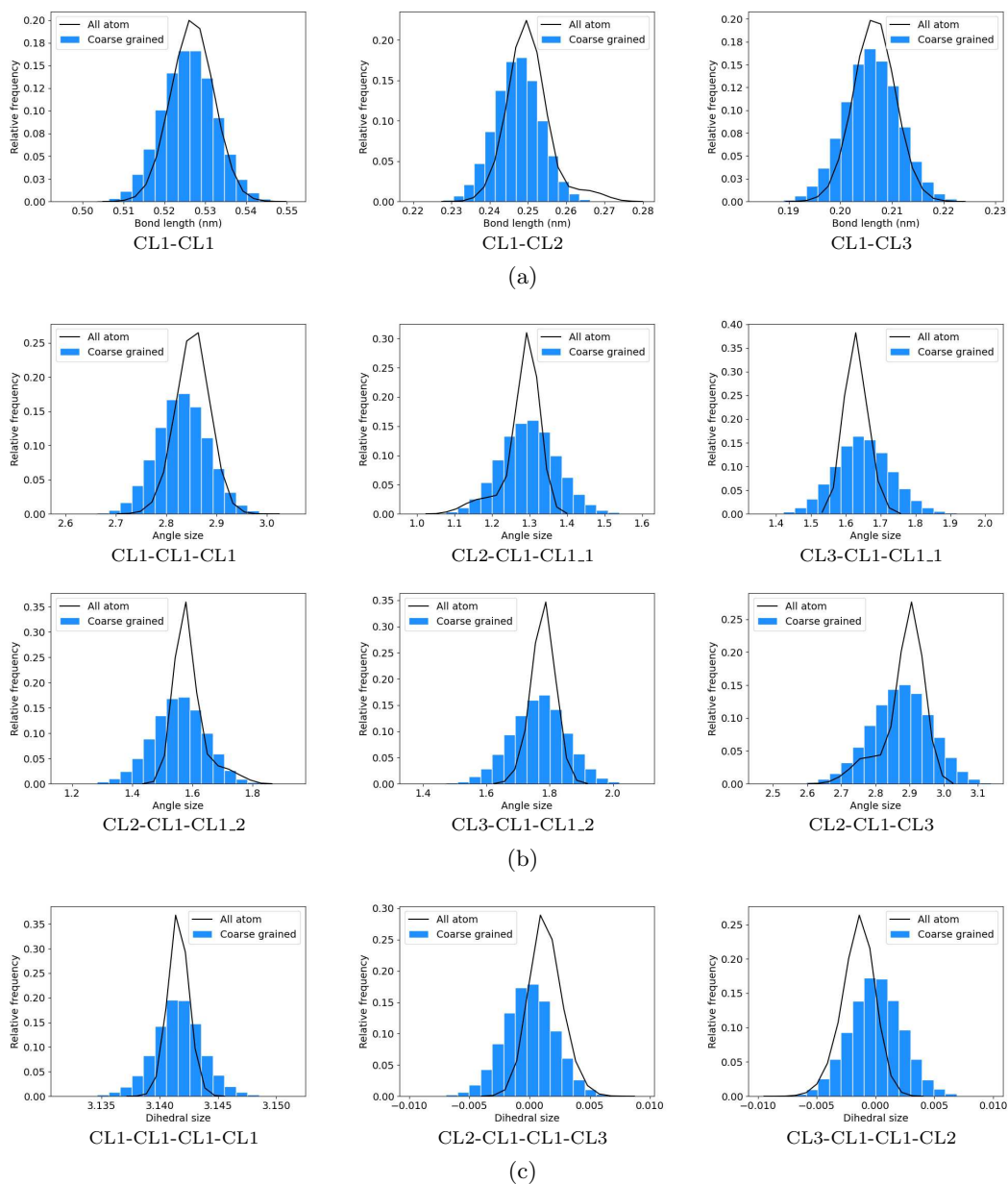


Figure S5: Comparison of bonded geometry parameter distributions. (a) Bond length distributions. (b) Angle size distributions. (c) Dihedral size distributions. These data are deprived from equilibrium CNC simulations of CG models and mapped AA models. Bonded geometry parameters are well preserved in this CG model with errors less than 2%, but the width of CG model is obviously larger due to smaller force constants for polymer stiffness. And the obvious secondary plateaus in the CL2-involved distributions are neglected.

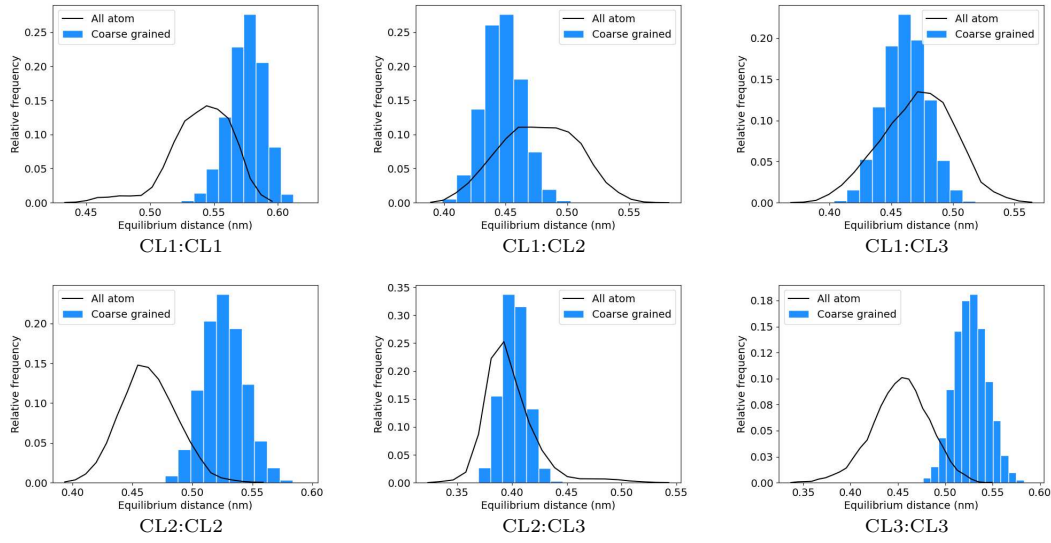


Figure S6: Comparison of nonbonded equilibrium distance distributions of pairs. These data are derived from equilibrium CNC simulations of CG models and mapped AA models. Corresponding to larger nonbonded distance coefficients than the estimated, equilibrium distances are often larger than expected to an acceptable extent. However, the resultant equilibrium distances of CL2:CL3 are not larger than all atom reference data, which elucidates the complexity of multiple particle models and helps us understand the enlargement of σ_{p23} .

Transverse stress-strain examples are provided to elucidate the reproduced transverse anisotropy of CNC (Figure S7). Radical distribution function, radius of gyration and root mean square deviation from slant CNC equilibrium simulations by CG models are compared with mapped AA models (Figure S8). These results better explain the effectiveness of this CG model.

Secondary summits

Harmonic bonded potential is appropriate for symmetric bonded geometry parameter distributions, which is the usual case for this model. However, Secondary plateau or secondary summit is included for bonded interactions with CL2 side chain beads involved Figure S9. They are caused by rotational degree of freedom of hydroxyls and are more obvious in single chain simulations, in which side chains are not restraint by hydrogen bonds. Our CG model chose to ignore the hydroxyl rotation for simplicity but may cause problems in other cases.

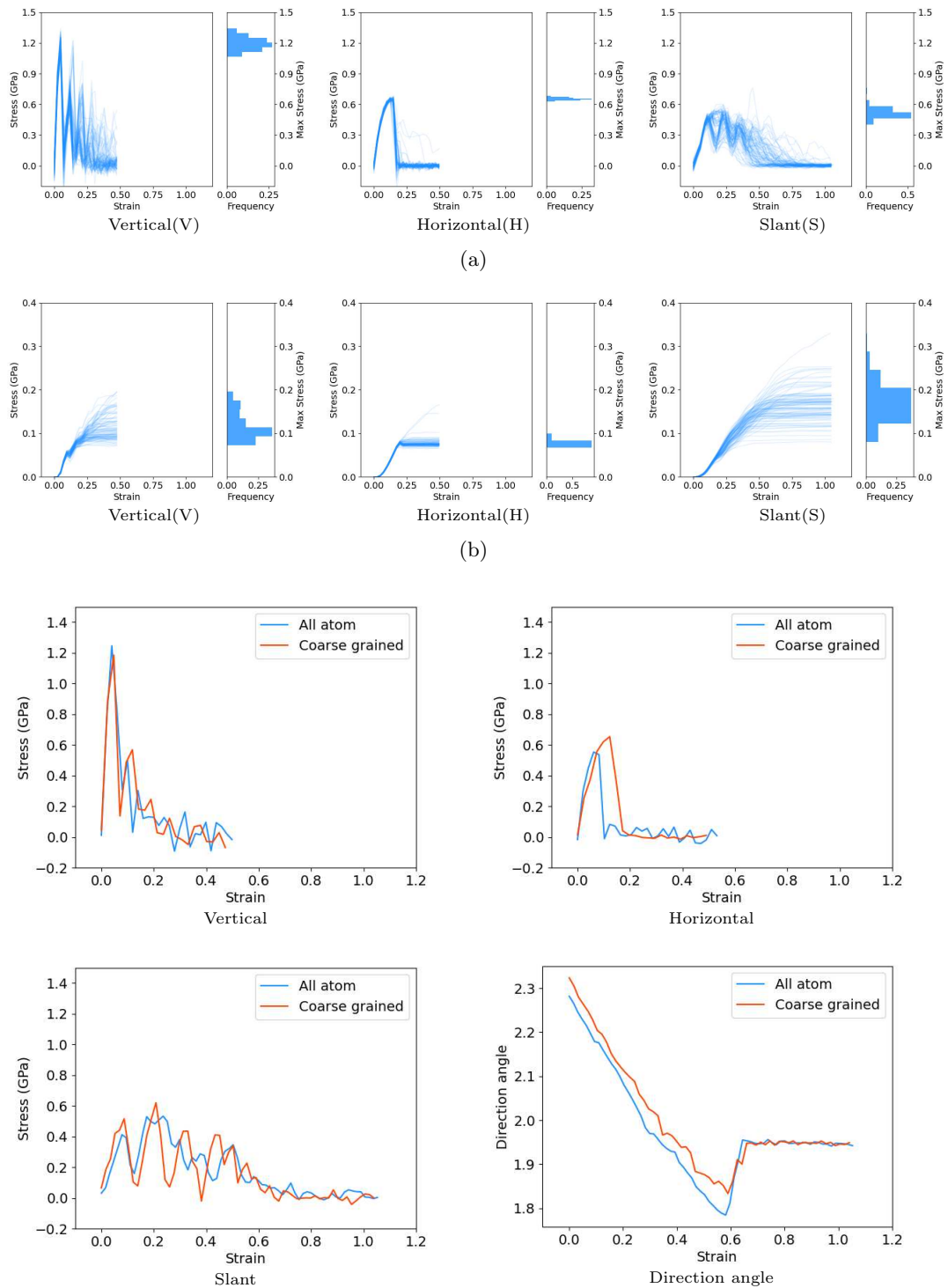


Figure S7: AA transverse stretch (a) stress-strain and (b) strain energy collections in characteristic directions at 10.0 nm/ns. Each collection contains 100 curves, and strength or toughness distribution is enclosed on the right. The secondary summits of Stress-Strain for vertical models are caused by horizontal dislocations. That means, fractured hydrogen bond layers rotate and reconnect to their nearby layers and break again. (c) Transverse stress strain examples in characteristic directions. Direction angle example is also attached for the slant model to describe frictional sliding quantitatively. Fragileness in vertical and horizontal models and ductility in slant model are all confirmed by example curves.

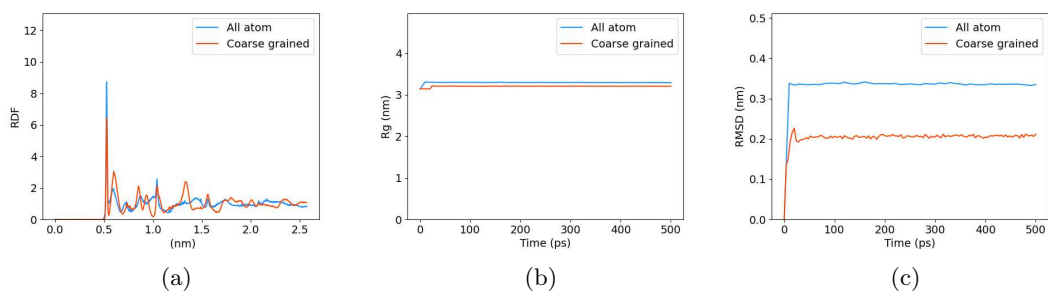


Figure S8: Other structure property examples. (a) Radial distribution function. (b) Radius of gyration. (c) Root mean square deviation. These data are derived from equilibrium CNC simulations of CG models and mapped AA models. They provide additional information to prove the structure similarity of CG models and AA models.

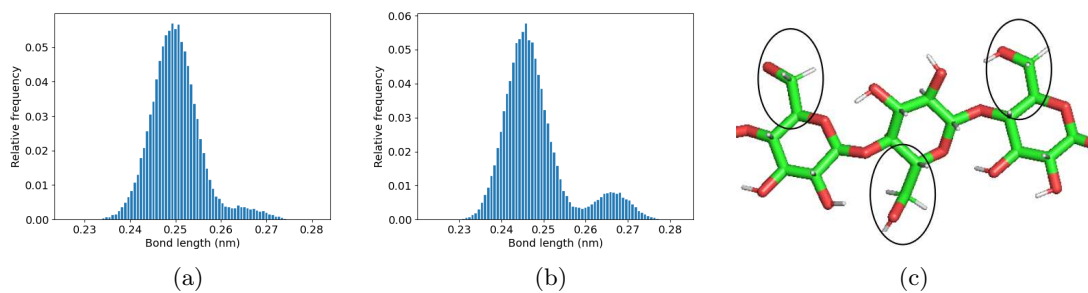


Figure S9: Secondary summits. (a) Mapped bond length distributions of CL1-CL2 from AA crystal simulations and (b) AA single chain simulations. (c) Secondary plateau of bonded geometry parameters are caused by rotational degree of freedom of side chain hydroxyls, especially for single chain simulations. The side chain hydroxyls are packed into CL2 beads. This means this CG model could not present this specific movement of cellulose which may be critical for some simulations.